DEPARTMENT OF PHYSICS
Institute for Astroparticle Physics

Novel Constraints on Millicharged Particles from Cosmic Ray Data

(Neue Limits für Millicharged Particles aus Experimentellen Daten Kosmischer Strahlung)

Master's Thesis
by

Maria Pokrandt

at the Institute for Astroparticle Physics

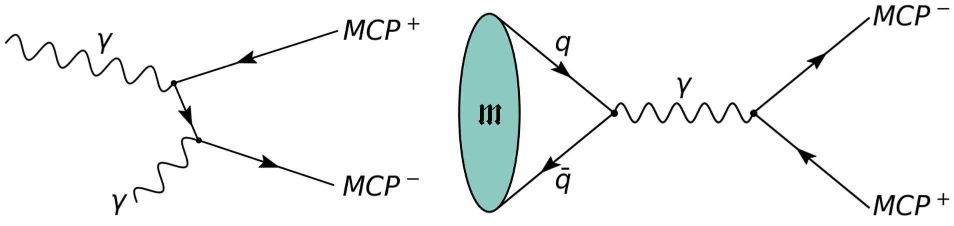

Reviewer: Prof. Dr. Ralph Engel
Second Reviewer: Dr. Ralf Ulrich

01. October 2020 – 01. October 2021

Erklärung zur Selbstständigkeit

Ich versichere, dass ich diese Arbeit selbstständig verfasst habe und keine anderen als die angegebenen Quellen und Hilfsmittel benutzt habe, die wörtlich oder inhaltlich übernommenen Stellen als solche kenntlich gemacht und die Satzung des KIT zur Sicherung guter wissenschaftlicher Praxis in der gültigen Fassung vom 24.05.2018 beachtet habe.

Karlsruhe, den 30.09.2021, ______________________________

Maria Pokrandt

Als Prüfungsexemplar genehmigt von

Karlsruhe, den 30.09.2021, ______________________________

Prof. Dr. Ralph Engel

Contents

Hypothetical millicharged particles (MCPs) as relics of beyond standard model theories have been researched and widely constrained in the last decades. Beside studies of MCPs in beam-dump experiments, researching MCPs in atmospheric particle cascades possesses great potential to be competitive with previous studies. Through implementing MCPs into the powerful cosmic-ray air shower simulation tool MCEq, we were able to compute atmospheric MCP fluxes in a mass range of $0.1\,\mathrm{GeV} \leq m \leq 100\,\mathrm{GeV}$ and charge range of $10^0 q_{el} \leq \varepsilon \leq 10^{-4} q_{el}$. In addition to producing MCPs by the widely studied neutral vector meson decay of η, ρ^0, ω, ϕ and J/Ψ, for the first time atmospheric photon pair production was considered as a production mechanism for MCPs. This approach opens the potential mass space of MCPs to higher masses than could have researched before. The propagation and energy losses of MCPs traversing through the Earth to a detector location have been thoroughly calculated through the utilization of the complex density model of the Preliminary Reference Earh Model (PREM). Finally, the theoretical detector signatures of MCPs through electron scattering have been calculated and compared to actual detector data. For this purpose, data from the dark matter experiment XENON1T and the neutrino detector Super-Kamiokande have been used to find new constraints on MCPs in the charge- and mass-space. The obtained limits are competitive with state-of-the-art MCP studies made by ArgoNeuT and milliQuan, and in a small region even show improved limits.

Hypothetische Teilchen namens "Millicharged Particles" (MCPs), die in einigen Erweiterungen des Standardmodells vorkommen, wurden in den letzten Jahrzehnten vielseitig untersucht. Neben der Untersuchung von MCPs in Beschleunigerexperimenten hat die stetige Verbesserung unseres Verständnisses für kosmische Strahlung dieses Feld als weitere Möglichkeit zur Untersuchung von MCPs hervorgebracht. Durch die Implementierung von MCPs in das Luftschauer-Simulationsprogramm MCEq, nicht nur über den vielfach untersuchten Mesonzerfall von η, ρ^0, ω, ϕ und J/Ψ Mesonen, sondern speziell durch die Implementierung von Photon-Paarproduktion, konnten wir den Fluss von MCPs in der Massenregion $0.1\,\mathrm{GeV} \leq m \leq 100\,\mathrm{GeV}$ und der Ladungsregion $10^0 q_{el} \leq \varepsilon \leq 10^{-4} q_{el}$ simulieren. Dieser weitere Produktionskanal eröffnet neue MCP-Massen, die so bis jetzt noch nicht untersucht werden konnten. Die Propagation von MCPs durch die Erde bis hin zu bestimmten Detektorstandorten und die dadurch entstehenden Energieverluste wurden durch die Verwendung des komplexen Dichtemodells des "Preliminary Reference Earth Model" (PREM) differenziert berechnet. Schließlich wurden theoretische Detektorsignaturen der MCPs mit echten Daten verglichen, und so neue Limits in der Ladungs- und Massenregion gefunden. Hierfür wurden Daten des Dunkle-Materie-Experiments XENON1T und des Neutrinodetektors Super-Kamiokande herangezogen. Die Ergebnisse dieser Arbeit sind konkurrenzfähig mit den aktuell besten Limits von ArgoNeuT und milliQuan, in einem kleinen Bereich sind die neuentdeckten Limits sogar noch besser.

1. Introduction

Physics as we know it today has come a long way and can explain almost all everyday phenomena. Despite the phenomenal success physicists are having with their predictions and explanations, the closer we come to the bedrock of underlying theories, the more anomalies we find that are still waiting to be understood. A popular example for such anomalies isn't even microscopic: Observations of the Milky Way's rotation and the movement of other galaxies (amongst other evidence) suggest the existence of large amounts of additional matter that we cannot see or detect, but that simply has to gravitationally affect our universe [1].

On smaller scales, we find anomalies even in the standard model of particle physics (SM), which is a fundamental and widely successful theory. A favored example are the observed non-zero masses of neutrinos, which were predicted to be massless in theory [2]. Also, the anomalous magnetic moment of the muon does not seem to match theoretical predictions [3]. With these being only examples, many outstanding problems in particle (astro)phyics remain [4].

For these reasons, a field called *physics beyond the standard model* (BSM) has gained large popularity in the last century [5]. In particular it is highly exciting to search for a connection of the SM to the "dark matter", which is currently assumed to be one of the most important problems of physics. As a result, some BSM theories predict new particles that differ in various ways from the known particles in the SM. One example for such particles are millicharged particles, or MCPs, which are the subject of this thesis.

Millicharged particles, as their name implies, are predicted to have lower charges than the SM charged leptons. However, their small charge makes them couple to SM photons and thus, the SM particles offer both production and observation channels. MCPs have been suggested by theories for some time now [6] [7], and researching their possible properties in the mass and charge range has become a popular niche in BSM physics.

The purpose of this thesis is to find additional competitive exclusion limits in the mass and charge plane of MCPs to the already existing bounds by improving the modelling of cosmic-ray induced production in the atmosphere and parasitically exploiting very-low-background detector data.

A popular attempt to study MCPs is trying to understand their behavior in particle accelerators and find exclusion limits through the accompanying detectors. Alongside large beam-dump experiments, MCPs could also be abundantly produced in cosmic particle cascades in our atmosphere. Particles originating in massive cosmic accelerators often reach us with ultrahigh energies and when interacting with atoms or molecules in our atmosphere, can cause enormous particle cascades. The production of MCPs in these atmospheric air showers is a promising alternative to accelerator experiments.

In this thesis the powerful cosmic-ray air shower simulation tool *MCEq* [8] was extended to simulate the behavior of hypothetical MCPs in these cascades. In addition to assuming

MCPs to be produced by neutral meson decay, for the first time also photon pair production has been implemented by using new models for electromagnetic air shower cascades. This is exciting, as photon pair production results in MCPs in a much wider and continuous mass range than assumed in previous studies, where only meson decay was considered [9] [10]. Furthermore, the photon-flux was never considered before for this purpose.

To achieve a much better validation of the obtained results, the muon flux above- and underground was simultaneously simulated and compared to existing data.

MCPs reaching the bottom of our atmosphere will propagate further through the Earth and eventually reach underground detectors. The sophisticated Earth density model of the *Preliminary Reference Earth Model (PREM)* [11] was used in this work to make refined assumptions about the resulting energy losses in the Earth.

Comparing the actual detector data to the predictions we can make for any given MCP flux reaching a detector, we can find limits for their possible masses and charges.

In this analysis, the published data of the detectors *XENON1T* [12] and *Super-Kamiokande* [13] were utilized to calculate new limits for MCPs. However, the method is applicable to any ultra-low-background detector data and can also be used to design future possibilities for maximum performance.

It is a key finding of this thesis that limits in a small area in the MCP mass and charge plane are found, that are even better than any other so far published results. This illustrates the relevance to further study exotic particle physics (and MCPs in particular) in cosmic-ray air showers as a competitive and promising tool.

The main improvements made in this study are the novel implementation of MCPs through photon pair production, the use of MCEq as a complex and versatile simulation tool, the consideration of the sophisticated Earth density model of the PREM and the simultaneous verification of our results using muons as a benchmark.

To provide a deeper insight into the current state of particle physics and the theoretical assumptions that lead to MCP predictions, a brief overview over the contemporary essentials will be given in chapter 2. Chapter 3 will introduce MCEq and explain the step by step process of bringing MCPs to artificial life through simulation. The effects of the propagation through the Earth of the predicted MCP fluxes will be illustrated in chapter 4. Finally, in chapter 5 we will look at detector data and generate new constraints in the MCP mass and charge plane.

2. Millicharged Particles

In this chapter, we will review the standard model of particle physics (SM) and its limitations. Hypothetical millicharged particles (MCPs) and their theoretical motivation will be briefly introduced and we will discuss possible mechanisms of producing MCPs through SM interactions.

2.1 Standard Model of Particle Physics

Before diving into physics beyond the standard model, let us revise its current state as shown in Fig. 2.1.

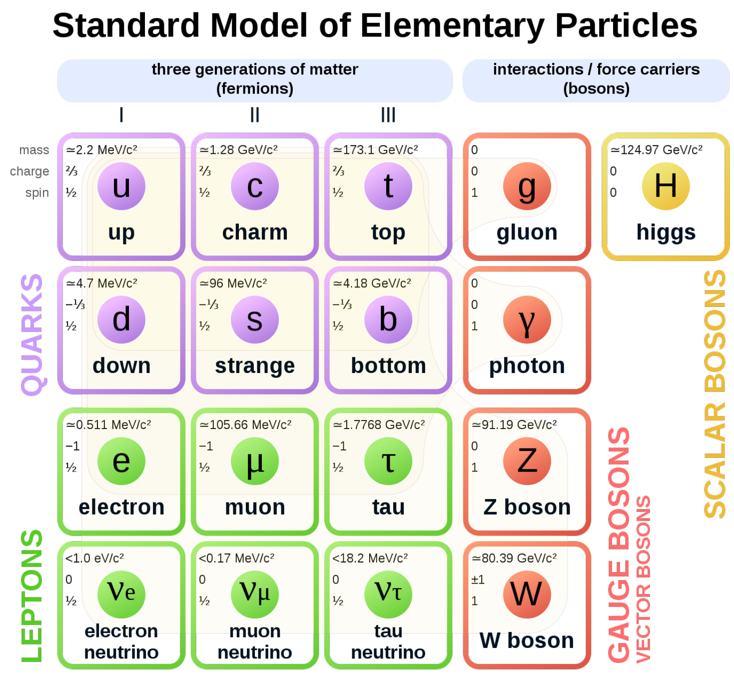

Figure 2.1: The standard model of elementary particles [14].

The well established standard model of particle physics classifies all particles that in today's understanding are assumed to be undividable, i.e. elementary particles. They are sorted into two basic groups: fermions, which make up all known matter, and bosons, which represent the fundamental interactions: gluons g are responsible for binding quarks within atoms through color charge, they mediate the strong interaction force as described by quantum chromodynamics (QCD). The photon γ carries out the force of quantum electrodynamics (QED) between electromagnetically charged particles or fields. The neutral Z- and charged $W^{\pm}$-bosons distribute the weak interaction, a force responsible for fermion transitions as for example seen in beta decay. These bosons are called gauge or vector bosons due to their spin of 1. The one scalar boson with spin 0 we know is the higgs boson connected to the origin of particle masses. Even though gravitational waves have been directly observed for the first time in 2015, the fourth fundamental force, gravity, does not yet have a representative particle in the SM. This shows how conceptually incomplete the SM still is and how necessary it is to look beyond and explore additional theories.

The group of fermions can again be divided into two subgroups: quarks and leptons. They are sorted into three so called generations, which contain particles with similar properties, that become heavier with each generation. For quarks, the positively charged group is composed by the up quark with an electromagnetic charge of two positive thirds of an electron charge and its heavier cousins, the charm quark and the top quark, which is the heaviest of all elementary particles. The negatively charged conjugate is the down quark with only one third of an electron charge, the heavier generations are called strange and bottom quark. Those charges of one and two thirds of an electron charge are presumed to be the most elementary charges known in the SM. The SM $U(1)$ gauge theory generally allows any small number charges, but we have not seen quantized charges other than $n \times q_d = n \times e/3$ yet. This charge quantization, though it is a fundamental and widely recognized assumption in particle physics, has not yet been proven unalterable and in this thesis, we will assume this principle to be broken.

The last group, leptons, contain the electron with an electromagnetic charge of one, its heavier counterparts muon and tau, as well as the three electromagnetically neutral and really light, altough not massless, neutrinos. All leptons interact with the weak force through $W^{\pm}$ and Z bosons. Electrons, muons and taus also interact with the electromagnetic force through photon interactions [15].
This interaction as well as the group of leptons will become important in the next chapter, where a new, hypothetical lepton-like particle called "Millicharged Particle" will be introduced.

2.2 Why extend the Standard Model?

As of today the standard model is remarkably successful in explaining the majority of phenomena seen in particle physics. Of course, since it is only a theory, a number of anomalies remain. The magnetic moment of the muon, for example, shows inconsistencies that can not yet be explained. Also, we find strong evidence for huge masses of additional matter, called dark matter, in the universe. As of today, the particle composition of this dark matter is unknown. Another example, just to show how fundamental the limitations of the SM are, would be the origin of neutrino masses, which are a necessary value for neutrino oscillation, when our gauge theories behind the standard model would actually predict neutrinos to be massless.

So despite its outstanding effectiveness, the SM can not be the final explanation for all phenomena we observe, and physics beyond the standard model (BSM) is an inevitable and exciting field of interest in physics today.

Several such BSM-theories as eg. string theories [16] or supersymmetry theories [17] can contain additional particles. An approach to suggest additional gauge fields in the standard model has been made by *Okun, 1982* [6] and *Holdom, 1985* [7]. This could be a dark sector (DS) added to our standard model (SM), represented very simplified by the SM- and DS-Lagrangian term in equation 2.1, as well as a third kinetic mixing term of the two vector field strengths, respectively, which is described in ref. [18]:

$$\mathcal{L} = \mathcal{L}_{SM} + \mathcal{L}_{DS} + \frac{\kappa}{2}\mathcal{B}'_{\mu\nu}\mathcal{B}_{\mu\nu}. \tag{2.1}$$

If, in accordance, there was a second massless $U(1)$ gauge field, a dark photon would emerge [19]. The known SM fermions would by definition not couple to this dark photon, though new fermion-like particles coupling to both the dark photon as well as the regular SM photon remain possible. The wave function renormalization of a theory with two $U(1)$ fields can be nondiagonal, which means that the fermions of one $U(1)$ are not bound to be charges with integer multiples of the charge scale of the other $U(1)$ field. In conclusion, depending on the symmetry breaking pattern in the dark sector, new fermions can experience a shift in charge quantization by a factor ε, that can basically be arbitrarily small. Even though we would expect to see this effect at high energy scales, these ε charge shifts can even persist down to lower energy scales if the dark vector field is massless.

We call these new arising fermions millicharged particles and in this work will refer to them as MCPs. For the sake of completeness, it should be emphasized that a dark photon is not necessarily required for MCPs and there are other ways of suggesting new fermions like MCPs.

2.3 Minimal MCP Model

We base our research on a so called *minimal MCP model* that makes only two assumptions:

- Millicharged particles couple to the SM photon with a fraction of an electron charge $q_{MCP} = \varepsilon \cdot q_{el}$ with typical values of $\varepsilon \ll 1$.
- We assume MCPs to have an infinite lifetime $\tau = \infty$, which means that they are stable particles at least on distance scales of our Earth.

With these assumptions, we recieve a lepton-like particle, whose mass depends strongly on the underlying theory. By keeping the model presumptions simple, we can make the most general and robust probes for finding simultaneous 2D constraints on MCP mass and charge. A wide variety of MCP masses ranging from $10^{-15}\text{eV} < m < 100\,\text{GeV}$ have been suggested and tested down to $\varepsilon \approx 10^{-6}$ or less and have been widely excluded [20]. Through those researches, the range of both the particle mass as well as the charge diminishing factor ε have been constrained as shown in Fig. 2.2. Traditionally, the search for MCPs was driven by beam-dump experiments, though in recent years also cosmic-ray driven searches have emerged due to novel tools and a better understanding of cosmic-ray uncertainties. These searches for MCPs in cosmic rays and cosmic air showers have become competitive and remain extremely promising.

2.4 Current Constraints on MCPs

To determine the region of interest in the mass and charge parameter space, we take a look at current constraints on millicharged particles.

In the parameter space of masses lower than 5 keV, the range of $10^{-14} \leq \varepsilon < 1$ has already been strongly constrained by collider experiments and astrophysical and cosmological observations. For slightly higher masses up to $\sim$ MeV, charges higher than $\varepsilon = 10^{-8}$ can be ruled out. Masses over a TeV can be excluded by dark matter searches, so millicharged particles are still possible in a mass range of MeV $< m <$ TeV [21]. Fig. 2.2 shows current constraints made at the mQ millicharged particle search at SLAC [22], the ArgoNeuT fixed target experiment at Fermilab [23] and beam-dump collider experiments [24].

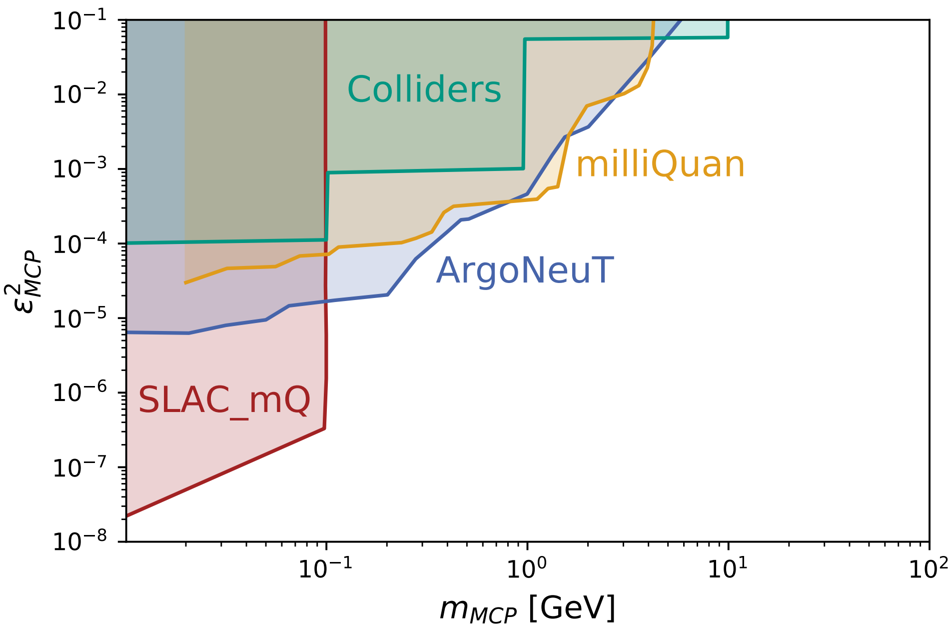

Figure 2.2: Current constraints on millicharged particles, data taken from [9] and [25]. Shown are constraints from SLAC [22], ArgoNeuT [23], milliQuan demonstrator [25] and collider experiments [21][24].

This figure shows, that it is most promising to focus on a mass space of 0.1 GeV to 100 GeV, and a charge space of $10^{-4} < \varepsilon < 1$.

The constraints made from ArgoNeuT data were published last year and set the current state-of-the-art limits in this mass and charge region. In this thesis, we will demonstrate that with studies of millicharged particles in cosmic-ray air showers, we can even achieve slightly better limits than ArgoNeuT in a certain parameter space. Also, this illustrates that in the near future, with both new beam-dump and also cosmic-ray/dark matter experiments upcoming, there is some cmopetitiveness and complementarity in the search for MCPs with the beam-dump and cosmic-ray experimental data.

2.5 Production Channels for MCPs

To be able to probe the existence of MCPs, we are going to introduce two possible production mechanisms. Neutral vector meson decay has been widely used to obtain MCP fluxes in previous research. However, there are significant uncertainties in the modelling of meson fluxes in the atmosphere, and we will employ state-of-the-art modelling in this work. Atmospheric photon pair production, as a second production channel, is even harder to predict, since atmospheric models are very expensive. This thesis provides the first attempt for an overall consistent approach, including both vector meson and photon pair production. A combination of the two production channels results in an improved analysis.

In this chapter, the production channels will be briefly explained. Their actual utilization can be found in chapters 3.4 and 3.5.

2.5.1 Vector meson decay

Millicharged particles, as they are charged leptons, can be assumed to be produced by meson decay. [9] Neutral mesons $\mathfrak{m}$ can decay into muon pairs via photon interaction through simple two-body-decays as shown in Fig. 2.3.

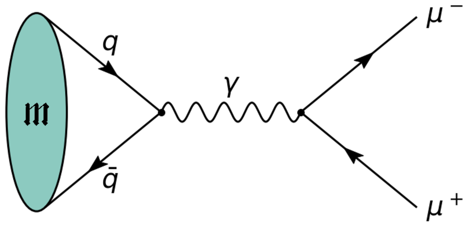

Figure 2.3: Feynman diagram of a q$\bar{\text{q}}$ meson decaying into a $\mu^-\mu^+$ pair through photon interaction.

The neutral pseudoscalar η meson as well as the neutral vector mesons ρ^0, ω, ϕ and J/Ψ can decay and produce a $\mu^-\mu^+$ pair with the respective branching ratios (BR) listed in table 2.1, as well as the meson mass and the maximum MCP mass that can be achieved by meson decay. A larger branching ratio leads to a higher production of MCPs in the possibly achievable mass range.
These five mesons have been chosen to be included in the production of MCPs in this work. MCPs that could come from the next lightest neutral meson, the π^0 meson with $m_{\pi^0} \approx 135\,\text{MeV}$, could only recieve a mass of $< 0.1\,\text{GeV}$ and are therefore out of bounds of our range of interest. Heavier mesons such as the Υ-meson can not be included in our simulation because they are not yet in our simulation tools particle repertoire. They are produced very rarely in our atmosphere, but a future inclusion will allow an extension of the analysis to even higher MCP masses. Though, they could be included as production channels for a more detailed study in the future.

Table 2.1: List of neutral mesons and their properties for pair production [26]

meson $\mathfrak{m}$	$m_{\mathfrak{m}}$ [MeV]	$\text{BR}_{\mathfrak{m}\to\mu^-\mu^+}$ [%]	$\text{m}_{MCP,max}$ [GeV]
η	547.862 ± 0.017	$(5.8 \pm 0.8) \times 10^{-6}$	0.274
ρ^0	775.26 ± 0.25	$(4.55 \pm 0.28) \times 10^{-5}$	0.388
ω	782.65 ± 0.12	$(7.4 \pm 1.8) \times 10^{-5}$	0.391
ϕ	1019.461 ± 0.016	$(2.86 \pm 0.19) \times 10^{-4}$	0.510
J/Ψ	3096.900 ± 0.006	5.961 ± 0.033	1.548

The branching ratio of MCP production from meson decay can be derived by 2.2, so the respective branching ratios depend both on the MCP mass and charge factor ε [27][28] as

$$\frac{BR_{\mathfrak{m}\to MCP^{\pm}}}{BR_{\mathfrak{m}\to\mu^-\mu^+}} = \varepsilon^2\sqrt{\frac{1+4m_{MCP}^2/m_{\mathfrak{m}}^2}{1+4m_{\mu}^2/m_{\mathfrak{m}}^2}}\,\frac{1+2m_{MCP}^2/m_{\mathfrak{m}}^2}{1+2m_{\mu}^2/m_{\mathfrak{m}}^2}. \tag{2.2}$$

The ratio between $BR_{\mathfrak{m}\to MCP^{\pm}}$ and $BR_{\mathfrak{m}\to\mu^-\mu^+}$ depends on ε^2 and a term depending on the respective masses m_{MCP}, m_μ and $m_{\mathfrak{m}}$.
With these assumptions, we can utilize $\mathfrak{m}\to\mu^-\mu^+$ decay as a template for MCP production.

In addition to neutral meson twobody-decays, *Dalitz*-decays such as $\mathfrak{m}\to\gamma\,\mu^-\mu^+$ could also be considered as production channels for MCPs. Their contribution to the MCP flux in atmospheric showers is considerably smaller, so they are not included in our conservative analysis. A study including Dalitz-decays can be found in ref. [27] and [29].

2.5.2 Pair production

Another way of obtaining lepton pairs like $\mu^-\mu^+$ is through pair production as shown in Fig. 2.4 and described in ref. [30].

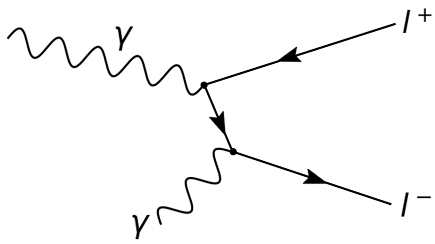

Figure 2.4: Feynman diagram of pair production of a lepton pair

The cross section of this process can be expressed by the *Maximon equation* and is essentially of the order $Z^2\alpha r_l^2$ with the charge number Z, Feinstruktur constant $\alpha\approx\frac{1}{137}$ and the classical radius r_l^2 of the produced lepton. Consequentially, the cross section of millicharged particle production through pair production depends on the charge diminishing factor ε as ε^2 and on the lepton radius with $r_l = e^2/(4\pi\varepsilon_0 mc^2)$. This radius can be scaled to millicharged particle production through the mass ratio of a known lepton mass m_l and the mass of the MCP m_{MCP}, causing the cross section to adjust with $(m_l/m_{MCP})^2$ [31].

In conclusion, the cross section of this production process for MCPs can be developed from muon pair production as follows:

$$\sigma_{\gamma\to MCP^+MCP^-} = \varepsilon^2\left(\frac{m_\mu}{m_{MCP}}\right)^2\sigma_{\gamma\to\mu^+\mu^-}. \tag{2.3}$$

As we can see, the ratio between the two cross sections $\sigma_{\gamma\to MCP^+MCP^-}$ and $\sigma_{\gamma\to\mu^+\mu^-}$ depends, again, on ε^2 and a term depending on the two masses m_μ and m_{MCP}. In the same way, MCPs could be produced from Z-boson pair production as $Z\to MCP^+MCP^-$. This production channel could be included in a future analysis to increase the flux of MCPs at higher masses even more, but since the atmospheric Z-boson flux is neither very well understood nor incorporated in the simulation environment we utilize, it is not going to be considered in this work.

In addition to the presented production channels, other more exotic ways of obtaining MCPs can be thought of, such as Drell-Yan processes or high energy higgsplosion events. Though they could be implemented in a future analysis, they are not dominant and our approach remains conservative in using only the selected production channels, which represent the major contributions to the atmospheric MCP flux.

3. Implementation of MCPs into MCEq

To observe atmospheric millicharged particle fluxes, in this chapter we are going to explain the process of implementing MCPs into the cosmic ray air shower simulation tool MCEq. Though MCP fluxes have been probed at colliders in laboratories, our approach is to calculate and simulate MCP fluxes in the atmosphere. Cosmic rays have a variety of advantages over collider experiments, such as possibly very high primary collision energies and the mere quantity of collisions happening per time and area unit. Furthermore, the idea is to reuse the data of deep underground neutrino and dark-matter detectors with extremely low background rates for the search of excess scattering from atmospheric MCPs. The technological advancement and size scaling of these detectors will allow very sensitive searches for MCPs.

3.1 Cosmic Particle Showers

When cosmic rays propagate through the universe, they may run across planet earth on their way. These primary particles consist of $\sim 90\%$ protons, 9% helium nuclei and 1% heavier ionized nuclei. Due to massive cosmic accelerators like supernova remnants, primary particles can reach very high, even ultrarelativistic energies of up to 10^{20}eV. They interfere with particles (atoms, molecules) in our atmosphere before they can reach the earth's surface. Such collisions between primary and atmospheric particles can be viewed as fixed target collisions, similar to proton beam dump collisions, in which the primary particles can evoke many other secondary particles, that cause further cascades on their way down the atmosphere. A schematic air shower cascade is shown in Fig. 3.1.

The main particle interactions can be divided into hadronic and leptonic interactions. The hadronic component is made up by nuclear fragments like protons and neutrons, neutral hadrons and charged mesons like pions or kaons. The leptonic component contains muons and neutrino interactions and a solely electromagnetic component with a main outcome of electrons, positrons and photons. The electromagnetic cascade loses energy mostly by pair production and bremsstrahlung. It can be detected in Cherenkov- and fluorescence detectors.

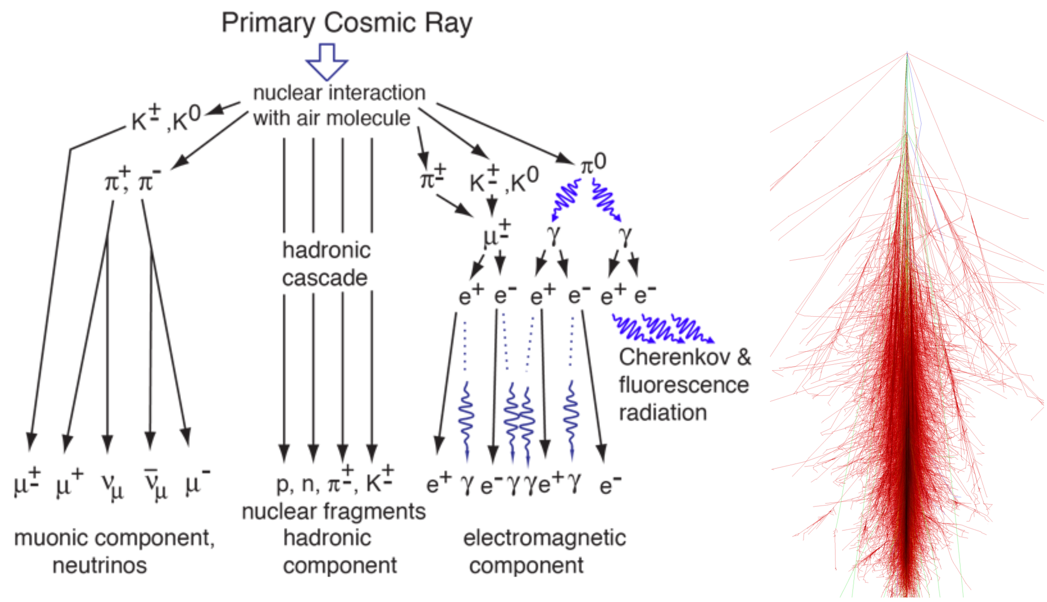

Figure 3.1: Schematic depiction of a cosmic particle cascade on the left [32]. On the right: particle shower simulated with CORSIKA with a 1 TeV primary proton [33].

The propagation of the particle cascade is driven by the primary particle energy and composition, as well as the atmospheric conditions. The total primary particle flux measured by various air shower detectors in their respective energy range is shown in Fig. 3.2. Several decreases in the graph can be seen at energies of around 10^{15}eV (*Knee*), $10^{17} - 10^{18}$eV (*2nd Knee*) and 10^{20}eV (Ankle).

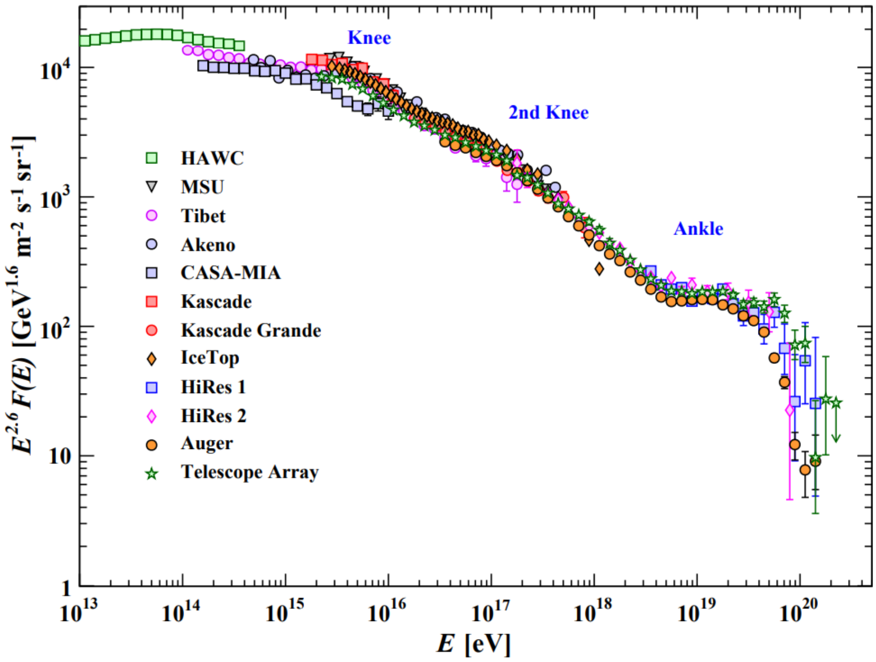

Figure 3.2: The total particle energy spectrum measured by several cosmic shower detectors. Image taken from [34].

Particles of energies up to 10^{18}eV reach us mostly from accelerators inside our galaxy.

The decrease of the energy spectrum in the *Knee* and the *2nd Knee* (also called *heavy knee*) regions is caused by the galactic acceleration processes of protons and heavier nuclei (up to iron nuclei) reaching their boundaries. Above the *Ankle*, the spectrum consists of particles coming from extragalactic origins, as the *Lamor-radius* of high-energy particles accelerated inside our galaxy exceeds our galaxies dimensions. This causes particles of energies over 10^{18}eV to no longer be magnetically confined and eventually leave our galaxy. The relatively abrupt dip in the spectrum at around 10^{20}eV is assumed to be due to the *Greisen-Zatsepin-Kuzmin limit*, a resonance interaction of primary particles with the cosmic microwave background (CMB) leading to a reduction of particle energy above a certain energy threshold of 5×10^{19}eV. Nonetheless, higher particle energies have been observed in rare occasions, for example by the Pierre Auger Observatory [35].

3.2 Cascade equations

To numerically compute cosmic particle showers, we need to express its particle content using cascade equations. We use the definitions and units as seen in and directly taken from [8], because those are the defined standards used in MCEq. We define the flux of a particle or particle group p as

$$\Phi_p = \frac{dN}{dA d\Omega dt} \tag{3.1}$$

with the number of particles N per unit area A, solid angle Ω and time t. The unit of the flux is therefore $\text{cm}^{-2}\text{sr}^{-1}\text{s}^{-1}$.

To differentiate between particle energies E, we introduce the differential flux

$$\frac{d\Phi_p}{dE} = \frac{dN}{dE dA d\Omega dt} \tag{3.2}$$

with resulting unit $\text{GeV}^{-1}\text{cm}^{-2}\text{sr}^{-1}\text{s}^{-1}$.

For expressing the flux of high energy particles p through matter, i.e. air, rock, etc. with the density ρ_{med} depending on the medium, we can espress the slant depth X in units g/cm^2 with

$$X(h) = \int_0^h \rho_{med}(l)\, dl \tag{3.3}$$

with the geometric trajectory l and height of interest h.

The resulting flux can then be written as

$$\frac{d\Phi_p(E,X)}{dX} = -\frac{\Phi_p(E,X)}{\lambda_{int,p}(E)} \tag{3.4a}$$

$$-\frac{\Phi_p(E,X)}{\lambda_{dec,p}(E,X)} \tag{3.4b}$$

$$-\frac{\delta\Phi_p(E_p,X)}{\delta E} \tag{3.4c}$$

$$+\sum_l \int_E^\infty dE_l \, \frac{dN_{l(E_l)\to p(E)}}{dE} \, \frac{\Phi_l(E_l,X)}{\lambda_{int,l}(E_l)} \tag{3.4d}$$

$$+\sum_l \int_E^\infty dE_l \, \frac{dN^{dec}_{l(E_l)\to p(E)}}{dE} \, \frac{\Phi_l(E_l,X)}{\lambda_{dec,l}(E_l,X)}. \tag{3.4e}$$

The first two sink terms describe the decrease of the total flux through interactions and decays with the interaction length in air $\lambda_{int,p}(E)$ and decay length $\lambda_{dec,p}(E,X)$ of a particle p. The third term subtracts the according flux due to energy losses in matter, and the last two terms represent the particle content produced by interactions with and decays from other parent particles. A broad study of calculating muon and neutrino fluxes through cascade equations was made by *Lipari* [36].

3.3 Matrix Cascade Equations (MCEq)

To compute cosmic air showers, we use the Matrix Cascade Equations (MCEq) simulation tool by *A. Fedynitch* [37]. It has been developed to calculate atmospheric lepton fluxes for IceCube and is useful to calculate the flux of various particles at any given height in the atmosphere. MCEq has a rather fast computing time because it is based on matrix calculations in Python. The particle content in a single shower is calculated stepwise through multiplication of particle content vectors and the respective cross section matrices. This chapter will contain a very brief introduction of the aspects of MCEq utilized for our purposes.

After installing and importing the mceq python package [38], MCEq can be initialized and basic parameters can be set, as the following code example taken from [39] shows:

```python
from MCEq.core import MCEqRun
import crflux.models as crf

# Initalize MCEq by creating user interface object MCEqRun
mceq = MCEqRun(

    # high-energy hadronic interaction model
    interaction_model='SIBYLL2.3c',

    # cosmic ray flux at the top of the atmosphere
    primary_model = (crf.HillasGaisser2012, 'H3a'),

    # zenith angle in degrees
    theta_deg = 0.0
)
```

We use a special version 1.3.1 of MCEq with an upgraded electromagentic simulation database, which allows us to make much more precise assumptions about the photon flux in the atmosphere. Throughout this work we will be using MCEq with the hadronic interaction model *SIBYLL 2.3c* [40]. SIBYLL is a well known and widely used standard Monte Carlo model for extensive air shower simulation. However, we also present results with *SIBYLL 2.3d* [41] and *DPMJET III* [42] in order to evaluate systematic uncertainties, which remain very limited.

As the primary particle model we primarily use the *HillasGaisser2012* model [43]. Again, cross checks with other primary models have not shown large systematic uncertainties. The zenith angle θ has to be given to MCEq as well. An angle of $\theta = 0°$ signifies primary particles originating from a vertical direction, whereas $\theta = 90°$ means a primary flux from a horizontal direction. Because the calculations made by MCEq depend strongly on the trajectory and length of the shower, computations with an angle of $\theta = 90°$ take significantly longer than those at a vertical zenith angle. In this work, we simulated showers from 0° to 90° in steps of 5°. The MCEq code also takes different density models as arguments. We choose to use the default model *BK_USStd*, which is an updated model of the US Standard Atmosphere [44] by *B. Keilhauer* and is also used by CORSIKA.
For our purposes, we now change the electromagnetic interaction model library as:

```
config.mceq_db_fname = 'mceq_db_lext_dpm191_v131_VM.h5'
config.em_db_fname = 'mceq_db_EM_Tsai_Full_v131.h5'
config.enable_em = True
```

This electromagnetic database contains pair production and bremsstrahlung of charged leptons as described in [30] and gives us the advantage of being able to calculate electromagnetic cascade fluxes much more precisely. The database is provided as a pandas DataFrame HDF5 file, which is a multi-dimensional storage option for complex data structures in Python. To initiate flux calculations, MCEq can be given a height grid to determine at which particular height the flux of interest needs to be calculated. The shown code examples are not complete and are meant only to show how MCEq is to be utilized in general:

```
n_pts = 50
X_grid = np.linspace(0.1, mceq.density_model.max_X,n_pts)
h_grid_1 = mceq.density_model.X2h(X_grid)
h_grid_2 = np.linspace(50 * 1e3 * 1e2, 0) # altitudes
   from 50 to 0 km (in cm)
mceq.solve(int_grid=X_grid)
```

Here, the `X_grid` is a list of 50 depth steps X along the cascade trajectory, while the `h_grid` can be directly mapped from the `X_grid` to obtain MCEq solutions at equivalent altitudes as in `h_grid_1` or be given as a list directly as in `h_grid_2`. The MCEq solver is then called by `mceq.solve()` with the respective height grid. To obtain particular differential particle fluxes at certain heights, the MCEq solutions have to be called with `mceq.get_solution()` as shown exemplary for muon and proton fluxes. The following two examples was made for a randomly chosen height of ~ 16 km just to show MCEq in action.

```
h = 10 # equals a depth of 16.006 km
muon_plot = mceq.get_solution('mu+', grid_idx=h, mag=3)
       + mceq.get_solution('mu-', grid_idx=h, mag=3)
proton_plot = mceq.get_solution('p+', grid_idx=h, mag=3)
```

A plot made for different particle fluxes to display what MCEq results look like is shown in Fig. 3.3.

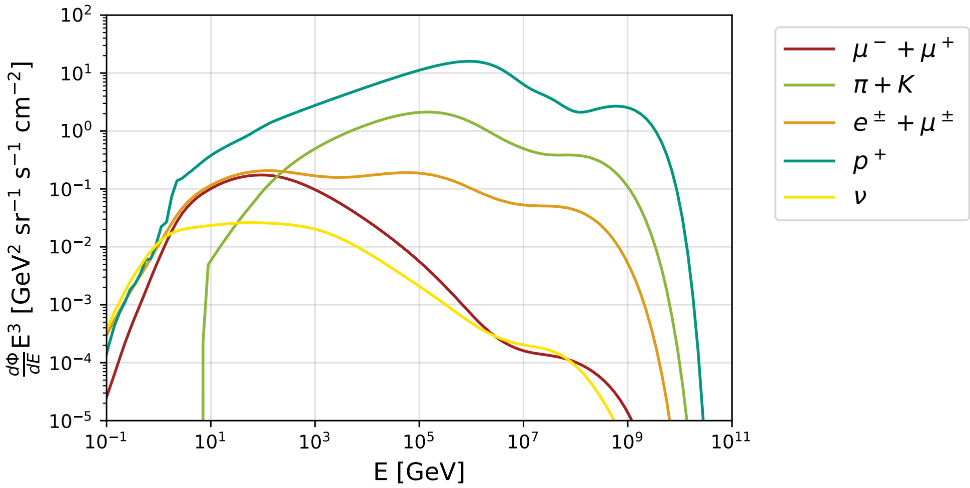

Figure 3.3: Exemplary energy spectra of various particles at an atmosperic height of $\sim 16\,\mathrm{km}$.

As seen in this example, we multiply the energy spectra with E^3 for better visibility at high energies.

MCEq uses an energy grid ranging from 10^{-1}GeV to 10^{11}GeV. The analysis in this thesis is going to be based on this energy range without any restrictions.

3.4 Implementation of MCPs in MCEq through pair production

To start with the implementation, the following steps are all going to be performed on a MCP charge of $q_{MCP} = \varepsilon \cdot q_e$ with $\varepsilon = 10^{-1}$. As we will see, MCPs of different charges can be scaled from these results, as described in 3.7. Also, we will show particle fluxes for a zenith angle of $\theta = 0°$, fluxes from different angles are going to be compared in section 3.7. Because of our assumption that MCPs are stable and will not decay, and because most MCPs are produced in the shower's high energy region close to the primary interaction, we see no relevant differences in the spectra for MCEq run at different zenith angles. Either way, our analysis does take the possibility of differences at various angles into account.

To implement millicharged particles into MCEq we use a Python package called EmCa, short for Electromagnetic-Cascades [45]. Like MCEq, it relies on matrix cascade equations, which makes it compute rather fast. EmCa can simulate electromagnetic cascades and can be used in combination with MCEq or standing alone. In its wide energy range (that is the same as the MCEq energy range), it includes ionization- and dielectric effects for low energies and the *Laundau-Pomeranchuk-Migdal* effect for high energies. The calculations for pair production and bremsstrahlung are based on the work of *Tsai* [30].

Unlike MCPs that are produced from neutral vector meson decay, and can therefore only recieve masses of up to half the parent meson mass, high-energy photons can produce MCPs in a very large mass range through pair production. Covering the interesting mass range clarified in 2.4 we choose to implement MCPs with the 25 masses shown in table 3.1.

Table 3.1: List of implemented MCP masses and their respective production channels

m_{MCP} [GeV]	production channels
0.1, 0.2	η, ρ, ω, ϕ, J/Ψ -decay, pair production
0.3	ρ, ω, ϕ, J/Ψ -decay, pair production
0.4, 0.5	ϕ, J/Ψ -decay, pair production
0.6, 0.7, ..., 1.5	J/Ψ -decay, pair production
1.6, 1.7, ..., 2.0, 5.0, 10.0, 20.0, 50.0, 100.0	pair production

Using EmCa for obtaining muon pair production matrices compatible with MCEq, we can adjust the mass of the produced lepton in the EmCa code and recieve different matrices for the resulting cross sections.

The production of matrices with EmCa has close to the same effect as adding the mass-factor as described in section 2.5.2, but has the advantage of already being in an MCEq compatible shape ready to use. Therefore, we will only need to scale the obtained matrices by a factor ε^2, since the mass effect has alredy been considered.

Fig. 3.4 shows the cross section matrix of muon pair production produced by EmCa as incidentally used in MCEq.

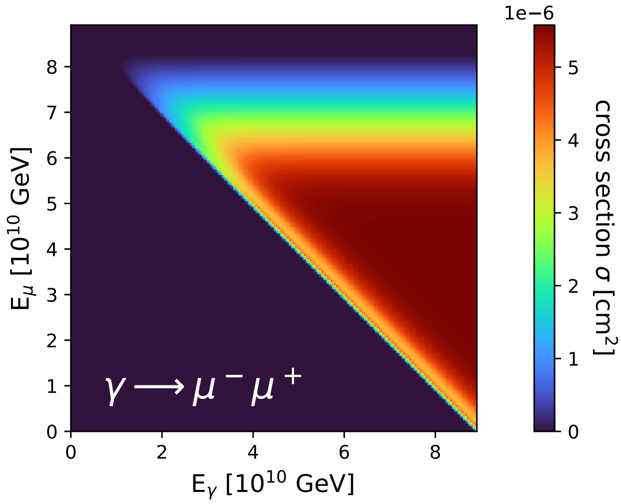

Figure 3.4: Cross section matrix for $\gamma \longrightarrow \mu^-\mu^+$ pair production produced with EmCa.

Two exemplary $\gamma \longrightarrow MCP^-MCP^+$ cross section matrices are shown in Fig. 3.5. For the minimal implemented MCP mass of 0.1 GeV (left side), note that the matrix looks similar to Fig. 3.4 due to the muon mass of ~ 0.1057 GeV being almost the same as the MCP mass. On the right side, the greatest implemented MCP mass of 100 GeV shows lower cross sections. Note the difference in the respective color scales.

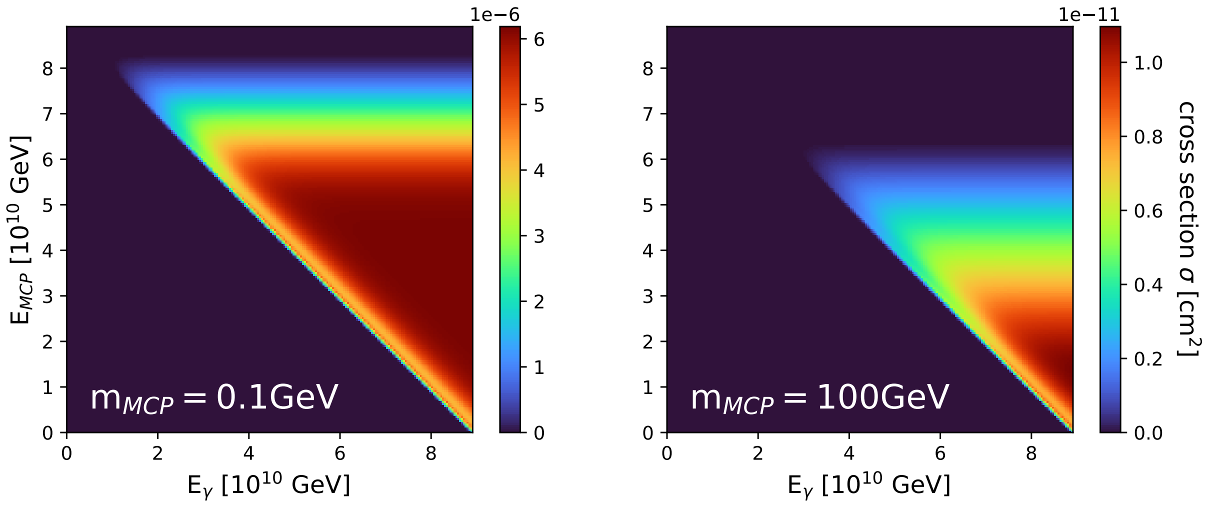

Figure 3.5: Respective cross sections shown for $\gamma \longrightarrow MCP^{-}MCP^{+}$ pair production for MCP masses 0.1 GeV on the left and 100 GeV on the right. Note that the scale on both colorbars differs.

Now that MCPs have some sort of primal production mechanism, we want to implement them into MCEq to be able to run simulations with the new particles. The implementation of a millicharged particle into MCEq takes the following steps:
We use the MCEq function `make_exotic_particle()`, which requires the respective MCP masses, MCP lifetime, particle name and PDG ID as parameters. The PDG ID is an individual ID according to a Monte Carlo numbering scheme [46]. We choose for the PDG IDs of MCPs to be numbers between 9000 and 9999, to not interfere with other particle IDs. All MCP masses considered in this thesis are added as individual particles at the same time. Thus, running MCEq once produces all the results for all MCP masses simultaneously. The assumption is, that the generation of MCPs is an extremely sub-dominant process in the shower, not affecting the remaining cascade at all. Also, MCPs fully decouple from the cascade once produced (similar to neutrinos). With `add_new_particle()` the new particles are added to MCEqs particle ID range. Using the `add_hadronic_production_channel()` function, we can submit the generated production matrices as shown in Fig. 3.5 to the MCP of the according mass and then add this process to photons as parent particles with `assert MCP_entry in gamma.hadr_secondaries`. The complete implementation code is shown below, though variable names have been changed for better understanding.

```
mceq.pman.add_new_particle(make_exotic_particle(mceq,
   MCP_mass, MCP_lifetime , MCP_name, pdg_id=MCP_PDG_ID))
MCP_cs = EmCa_mat.get((22,13))*epsilon**2
MCP_entry = mceq.pman[MCP_PDG_IDs[index]]
gamma.add_hadronic_production_channel(MCP_entry, MCP_cs)
assert MCP_entry in gamma.hadr_secondaries
```

The flux of photons in the atmosphere is shown in Fig. 3.6 for a primary zenith angle of $\theta = 0°$ and $\theta = 80°$.

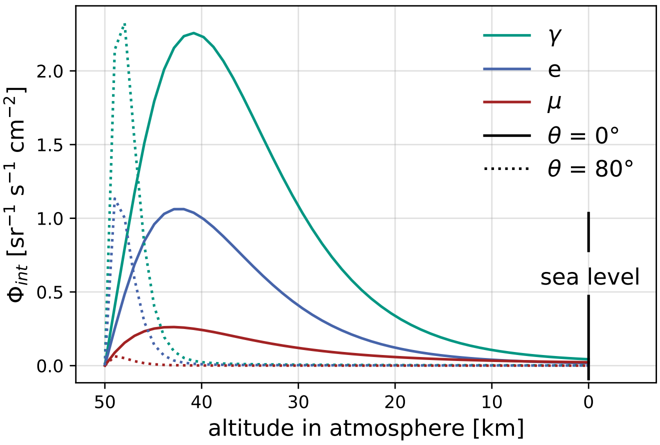

Figure 3.6: Photon, muon and electron integrated flux computed with MCEq at varying atmospheric heights. Shown for primary zenith angles $\theta = 0°$ in solid lines and in dotted lines for $\theta = 80°$.

The resulting energy spectrum of the MCP flux is shown in Fig. 3.7 for MCP masses 0.1, 1, 10 and 100 GeV at a primary zenith angle of $\theta = 0°$. Note that the x- and y-scale range very widely.

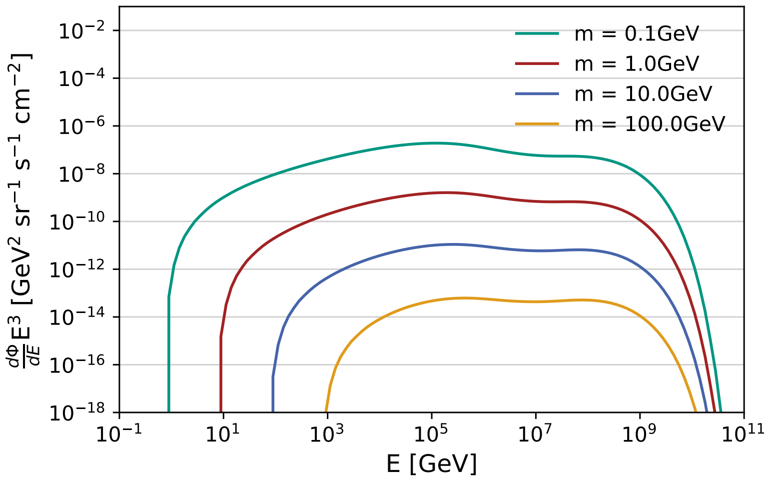

Figure 3.7: Differential fluxes at sea level for exemplary MCP masses 0.1, 1, 10 and 100 GeV from pair production at primary zenith angle $\theta = 0°$.

The integrated flux as a function of the MCP mass for the same zenith angle is shown in Fig. 3.8.

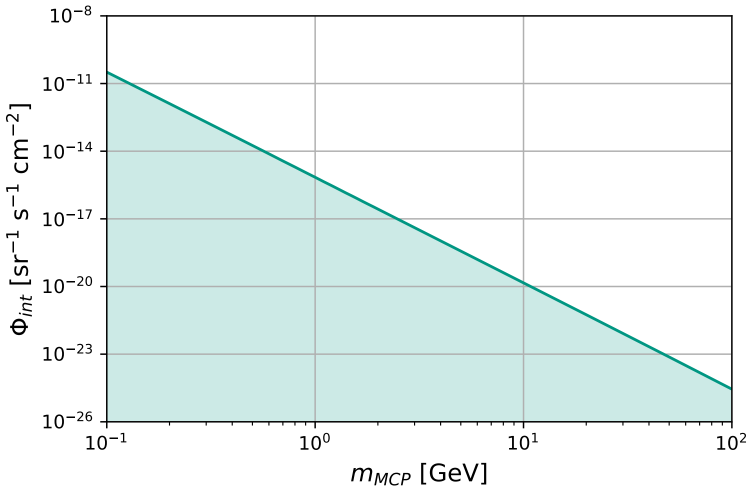

Figure 3.8: Flux at sea level for MCP masses at primary zenith angle $\theta = 0°$.

The total flux of MCPs can now be achieved by integrating the flux over all zenith angles as will be described in section 3.7.

3.5 MCPs from vector meson decay

Neutral vector mesons can produce lepton-antilepton pairs via dilepton decay as described in 2.5.1. When decaying in the rest frame with parent particle momentum $p = 0$, as seen in Fig. 3.9, the two emerging leptons have oppositely oriented momenta p_1 and p_2. In cosmic air showers, the parent meson has an initial momentum that can be much higher than its mass and is therefore $p \approx E$. The child particle momenta result to be quasi-collinear, as their momenta are much smaller than the parent momentum and can hence be neglected when the parent energy is high.

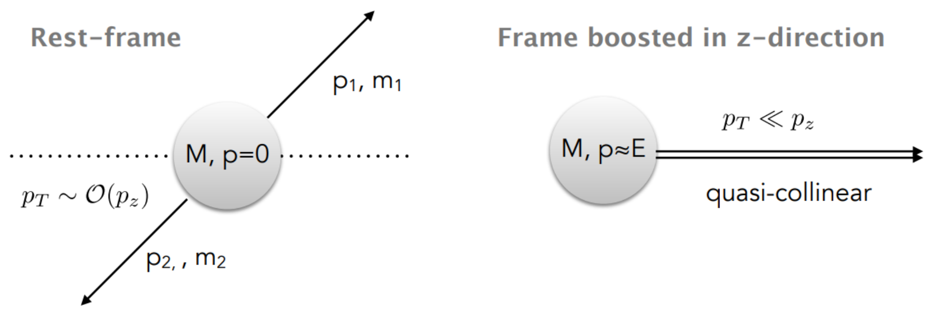

Figure 3.9: Schematic depicition of twobodydecay in the rest-frame vs. in the boosted frame. Figure taken from [8].

To implement this twobody decay into MCEq, we need to make production matrices similar to the ones we made to describe the pair production mechanism in the previous section.

The calculations are relatively trivial to where we use a range of parent particle energies in the MCEq energy range from 10^{-1}GeV to 10^{11}GeV, have them decay in a Monte Carlo simulation with several thousands of events and then shift the resulting momenta to the boosted frame. As a result, we recieve matrices as shown in Fig. 3.10.

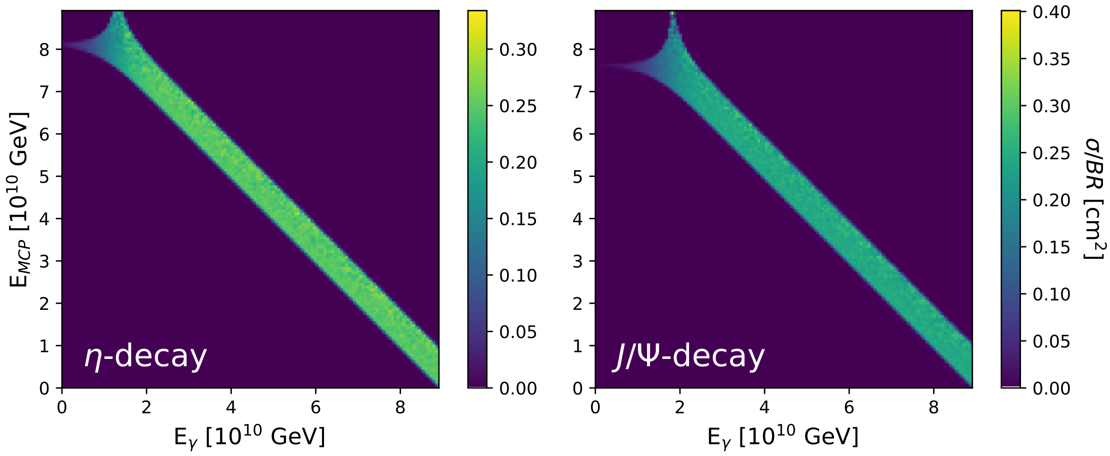

Figure 3.10: Exemplary matrices of twobodydecays of η-mesons to MCPs with a mass of 0.1 GeV on the left vs. twobodydecay of J/Ψ-mesons to MCPs with a mass of 0.5 GeV on the right.

These matrices still need to be multiplied with the branching ratios of the respective processes as described by 2.2 to receive the cross section matrices for neutral meson decay into MCPs. To show an example, the implementation of ϕ-meson decay for the MCP with mass index `m_idx` in MCEq looks as follows:

```
MCP_cs_phi = BR(phi)*decay_matrices[:,:,m_idx]
phi.add_decay_channel(mceq.pman[MCP_PDG_IDs[m_idx]],
   MCP_cs_phi, force=True)
```

The branching ratio is used as seen in table 2.1. The respective `MCP_PDG_IDs` depend on the MCP mass. With the MCEq function `.add_decay_channel()`, the decay channel of ϕ-mesons into MCPs is added.

The flux of various neutral mesons in our atmosphere is shown in Fig. 3.11. Note that the y-axis is scaled logarithmicly and heavier meson fluxes are much lower than lighter ones. This graphic is taken from [27], as the neutral mesons are implemented into MCEq as resonances only and their flux cannot easily be displayed using MCEq.

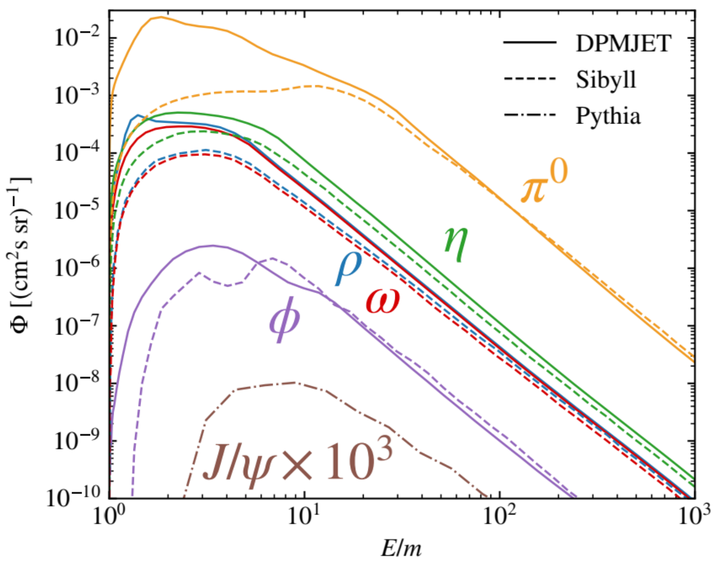

Figure 3.11: Flux of mesons produced in air showers using different cosmic ray interaction models DPMJET, Sybill and Pythia. Image taken from [27].

As a result, we receive additional MCP fluxes for MCPs of masses up to 1.5 GeV. The differential fluxes for MCPs of masses 0.1, 0.3, 0.5 and 1.5GeV are shown in Fig. 3.12.

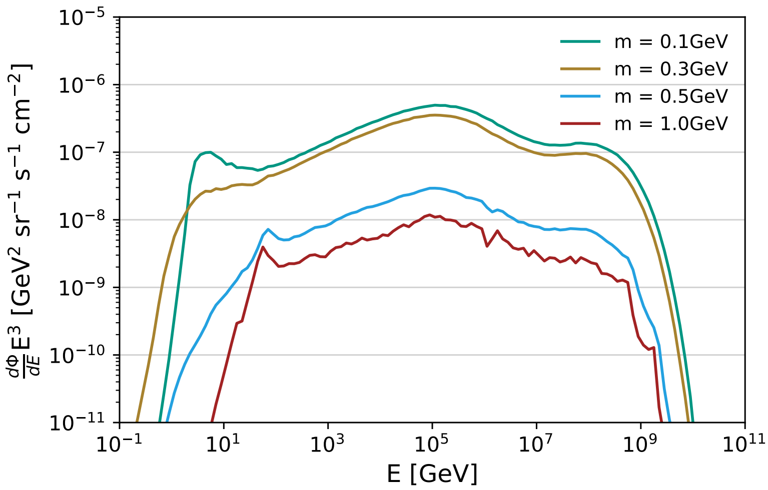

Figure 3.12: Differential fluxes at sea level for exemplary MCP masses 0.1, 0.3, 0.5 and 1.0 GeV from neutral meson decay at primary zenith angle $\theta = 0°$.

The several fluxes of MCPs in the MCEq energy range coming from each individual meson decay compared to the MCP flux from photon pair production can be seen in Fig. 3.13. The flux from ρ- and ω-decay are almost the same, because they almost have the same mass and $\mathfrak{m} \to MCP^{\pm}$ branching ratio.

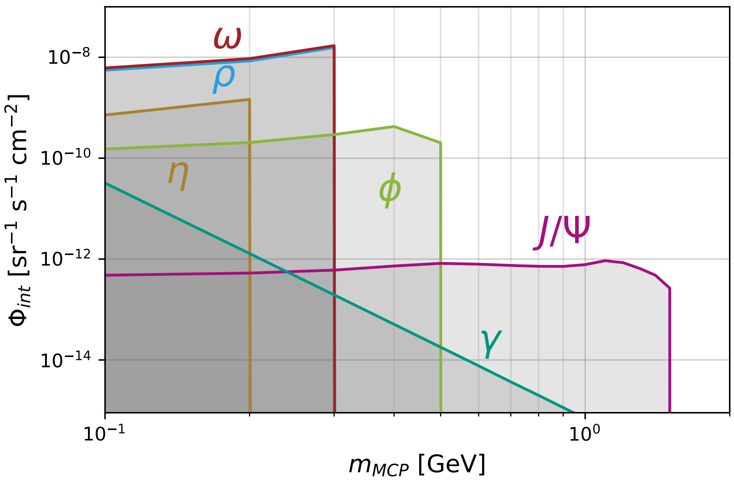

Figure 3.13: Flux of MCPs shown for each meson decay.

The total flux resulting from meson decay is finally shown in Fig. 3.14. The respective proportions from the individual mesons are shown in different colors.

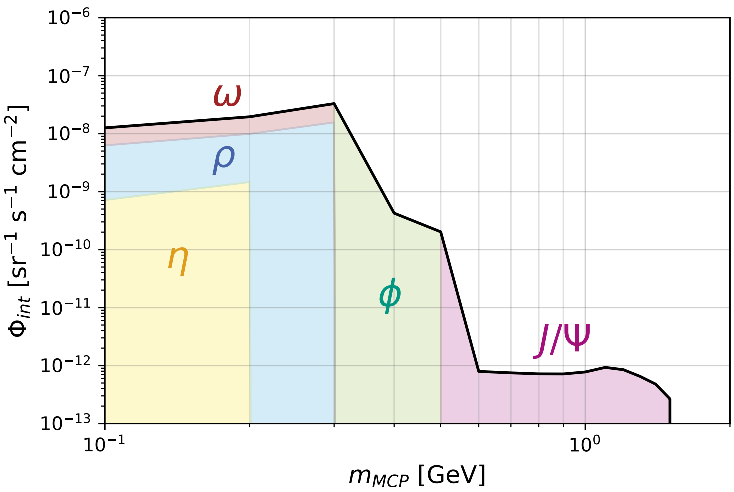

Figure 3.14: Total flux of MCPs from meson decay at primary zenith angle $\theta = 0°$. Highlighted in different colors are the respective proportions coming from different mesons.

Note, again, that the scales are logarithmic and fluxes from ρ and ω decay are about the same.

3.6 Energy loss in the atmosphere

Even though we assume MCPs to be stable and not decay into other particles, their passage through the atmosphere (and of course through matter in general) results in energy losses $\frac{dE}{dX}$ [47]. To determine the total energy loss of MCPs, we need to take a look at lepton energy losses in general, in particular muon energy losses. The basic reasons for lepton energy loss in matter are ionization losses characterized by the *Bethe-Bloch equation* and radiative losses such as bremsstrahlung, pair production and nuclear effects like muon hadroproduction [48].

The resulting stopping power for charged particles in matter can be summarized as

$$-\left\langle \frac{dE}{dX} \right\rangle = a(E) + b(E)E \tag{3.5}$$

with coefficients $a(E)$ representing the ionization losses as a function of energy and $b(E)$ being the summarized radiative losses $b = \{b_{brems} + b_{pair} + b_{hadr}\}$.

The ionization losses of MCPs, as the Bethe-Bloch formula is of the order z^2, can be directly scaled down from muonic ionization losses, which are already integrated in MCEq. The scaling factor depends on the MCP charge factor ε only as $a_{MCP}/a_\mu \propto \varepsilon^2$ and is therefore the same for all implemented MCP masses.
The radiative losses depend on the various processes differently as

$$\frac{b_{MCP,pair}}{b_{\mu,pair}} \propto \Big(\frac{m_\mu}{m_{MCP}}\Big)\varepsilon^2; \qquad \frac{b_{MCP,brems}}{b_{\mu,brems}} \propto \Big(\frac{m_\mu}{m_{MCP}}\Big)^2 \varepsilon^4; \qquad \frac{b_{MCP,hadr}}{b_{\mu,hadr}} \propto \varepsilon^2. \tag{3.6}$$

In our mass range of $\mathrm{m}_{MCP} > \mathrm{m}_\mu$, pair production is the leading behavior, and so the total energy loss from radiative processes can be summarized by Eq. 3.7 [49] as

$$\frac{b_{MCP,tot}}{b_{\mu,tot}} \simeq \frac{1}{2}\Big(\frac{m_\mu}{m_{MCP}}\Big)\varepsilon^2. \tag{3.7}$$

To implement the energy loss into MCEq we use `muon.dEdX`, which are the muonic ionization losses $a_\mu(E)$, multiply them by ε^2 and subtract (energy losses are defined as negative values by MCEq) the radiative losses b that we calculate as

$$b(m_{MCP}, E) = \frac{1}{2}\, b_\mu\, \varepsilon^2\, \Big(\frac{m_\mu}{m_{MCP}}\Big) \times E \tag{3.8}$$

with $b_\mu = 4 \times 10^{-6}\mathrm{GeVg}^{-1}\mathrm{cm}^2$ taken from [50].

```
mceq.pman[MCP].has_contloss = True
mceq.pman[MCP].dEdX = muon.dEdX * epsilon**2 - b(m_MCP)
```

The radiative losses differ for various MCP masses, two examples for $\mathrm{m}_{MCP} = 0.1\,\mathrm{GeV}$ and $\mathrm{m}_{MCP} = 100\,\mathrm{GeV}$ can be seen in dotted lines in Fig. 3.15. In conclusion, the total energy losses $-\langle \frac{dE}{dX} \rangle$ are shown in solid lines for MCP energies along the MCEq energy range.

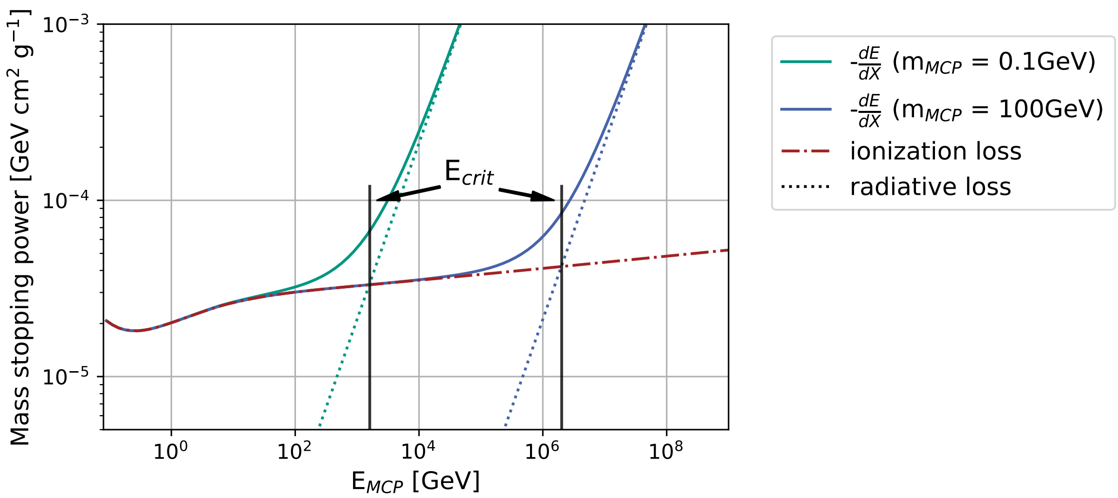

Figure 3.15: Mass stopping power $-\langle \frac{dE}{dX} \rangle$ in air shown in for MCPs with masses 0.1GeV (green line) and 100GeV (blue line) in the MCEq energy range. Ionization losses are represented by the red dash-dotted line, radiative losses are displayed by dotted lines. Critical energy is shown for both examples, on the left side of E_{crit} lies the Bethe-region, where energy losses mostly depend on the Bethe-Bloch formula. On the right side of E_{crit}, energy losses are dominated by radiative processes.

As a result, the energy losses of MCPs in the atmosphere lead to a loss in the differential energy spectrum shown in Fig. 3.16.

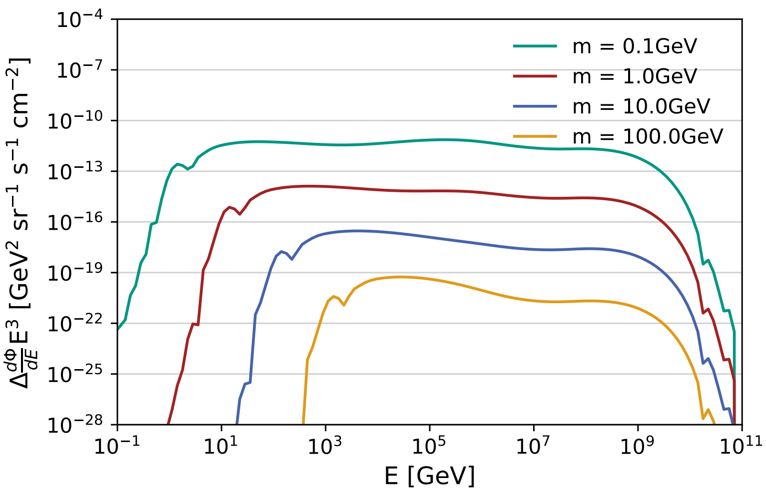

Figure 3.16: Losses in the differential flux spectrum through atmospheric energy losses. Note that the flux values are technically negative, because these are flux losses.

The differential flux losses are of the order 10^5 to 10^{10} lower than the differential flux itself, so the impact of the atmospheric energy losses on the MCP flux is invisibly low.

3.7 Flux of MCPs at sea level from MCEq for different ε and θ

As a result of the implementation of millicharged particles through photon pair production, neutral vector meson decay and also adding the energy loss $\frac{dE}{dX}$, the received differential flux $\frac{d\Phi}{dE}$ in the MCEq energy range is shown exemplary for zenith angle $\theta = 0°$ in Fig. 3.17.

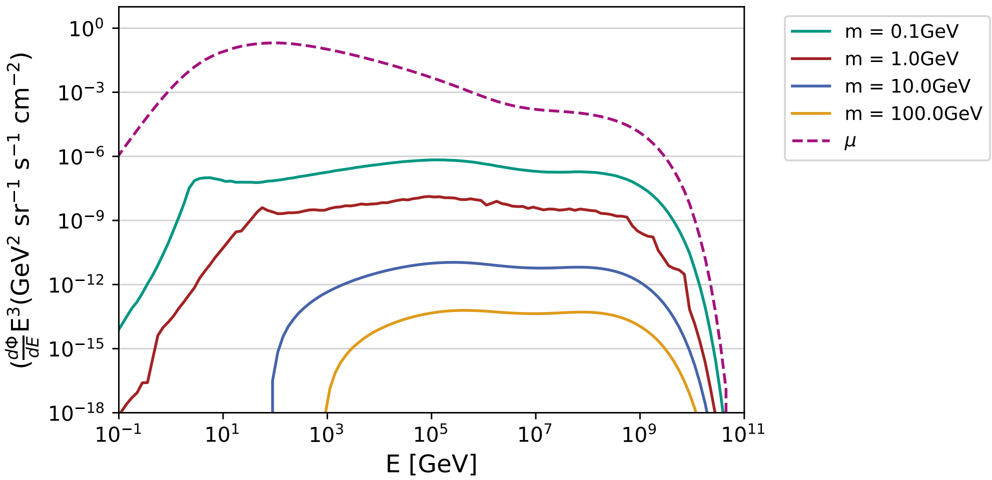

Figure 3.17: Differential flux spectrum for zenith angle $\theta = 0°$ and charge factor $\varepsilon = 10^{-1}$. For comparison, the muon flux for the same zenith angle is shown (dashed line).

Because MCP production happens mostly at the top of the atmospheric cascade, the zentih angle and therefore the total slant depth of the atmospheric trajectory hardly affects the flux of MCPs, as can be seen in Fig. 3.18.

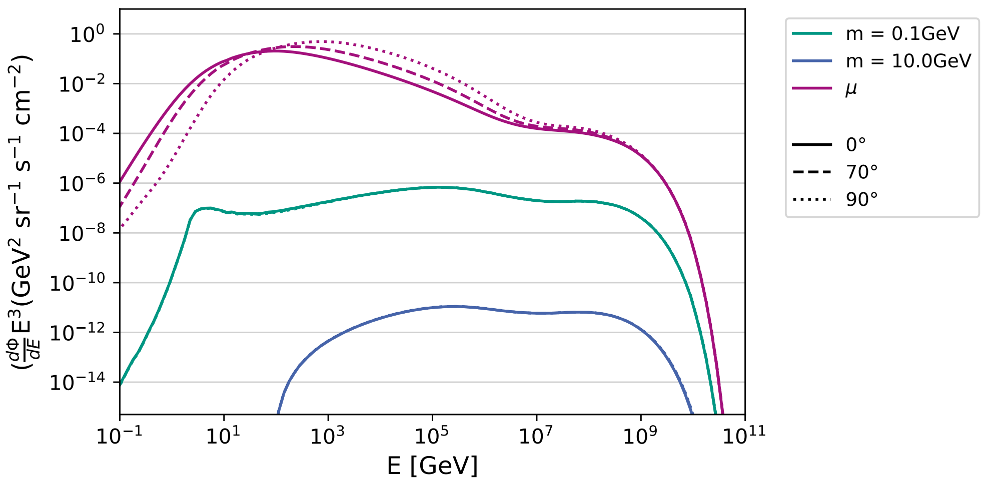

Figure 3.18: Differential flux spectrum for 0.1 GeV and 10.0 GeV MCPs with charge factor $\varepsilon = 10^{-1}$ at zenith angles $\theta = 0°$ (solid lines), $\theta = 70°$ (dashed lines) and $\theta = 90°$ (dotted lines). For comparison, the muon flux is shown at the same angles.

The total flux of particles per sr, s and cm^2 integrated over the MCEq energy range is shown in Fig. 3.19.

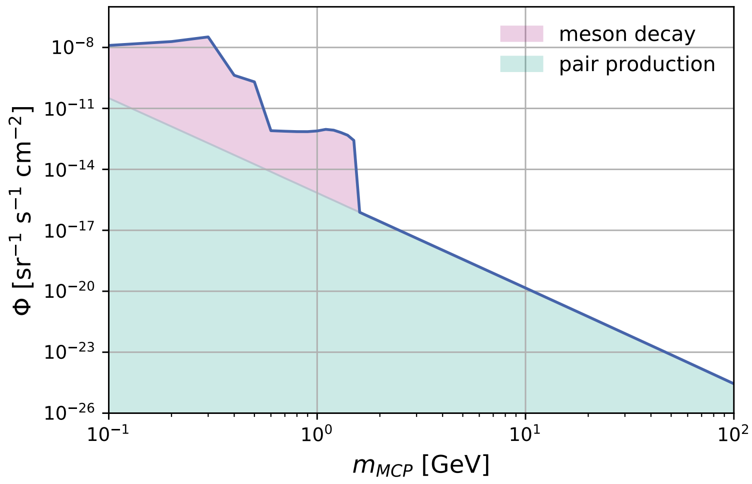

Figure 3.19: The total flux of MCPs. Contributions from meson decay and pair production are highlighted as purple and green areas.

Throughout the last chapters, we have assumed $\varepsilon = 10^{-1}$. Reviewing the equations leading up to Fig. 3.17, we notice that they all depend on ε as ε^2.

$$\varepsilon^2 \cdot \left(\frac{d\Phi_{MCP}}{dE}\right) = \varepsilon^2 \cdot \left(\frac{d\Phi_{MCP}}{dE}\right)_{pair} + \varepsilon^2 \cdot \left(\frac{d\Phi_{MCP}}{dE}\right)_{mes} - \varepsilon^2 \cdot \left(\frac{d\Phi_{MCP}}{dE}\right)_{dE/dX} \tag{3.9a}$$

$$\varepsilon^2 \cdot \left[\left(\frac{d\Phi_{MCP}}{dE}\right)_{pair} + \left(\frac{d\Phi_{MCP}}{dE}\right)_{mes} - \left(\frac{d\Phi_{MCP}}{dE}\right)_{dE/dX}\right]. \tag{3.9b}$$

We can therefore receive MCP fluxes of charges $\varepsilon_{new} \cdot q_e$ by simply rescaling a particular MCP flux of charge $\varepsilon_{scale} \cdot q_e$ by a factor $\zeta = \varepsilon_{new}/\varepsilon_{scale}$ as

$$\varepsilon_{new} \cdot \left(\frac{d\Phi_{MCP}}{dE}\right) = \zeta \cdot \varepsilon_{scale} \cdot \left(\frac{d\Phi_{MCP}}{dE}\right). \tag{3.10}$$

Fig. 3.20 shows the fluxes of 0.1 GeV and 10.0 GeV MCPs with charges of $q_{el} \cdot 10^{-1}$, $q_{el} \cdot 10^{-3}$ and $q_{el} \cdot 10^{-5}$.

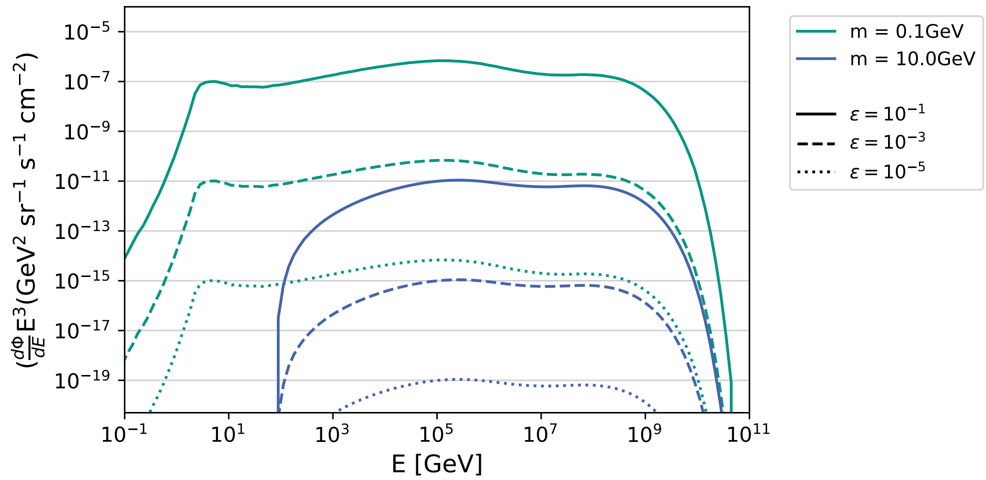

Figure 3.20: Differential flux spectrum for zenith angle $\theta = 0°$ and charge factors $\varepsilon = 10^{-1}$ (solid lines), $\varepsilon = 10^{-3}$ (dashed lines) and $\varepsilon = 10^{-5}$ (dotted lines).

3.8 Comaprison of MCP flux for different model assumptions

The systematic uncertainties of our analysis so far depend mostly on the used atmospheric density, primary and interaction models. In this chapter, we are going to look at the impact of different models on the current results for the MCP flux. The basic models will remain as explained in section 3.3, only the model of interest will be changed in the corresponding graphs.

In Fig. 3.21, the three interaction models *SIBYLL 2.3c* [40], *SIBYLL 2.3d* [41] and *DPMJET III* [42] are compared. Unsurprisingly, the two *SIBYLL* models show no differences, whereas the *DPMJET* model shows slight differences in the high energy range. The flux in the high energy range is decreasing rapidly, note that the flux shown here is multiplied with E^3, so the impact of these differences on the total results remains small.

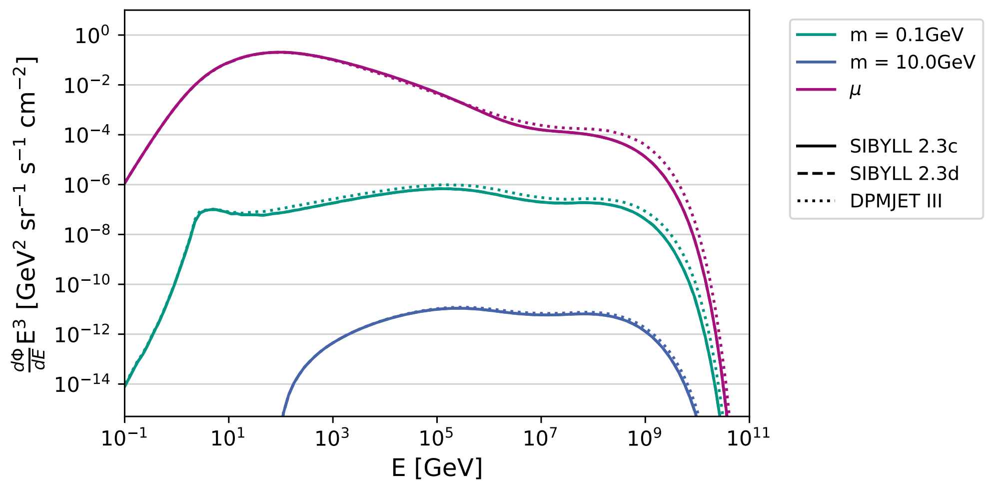

Figure 3.21: Differential flux spectrum for 0.1 GeV and 10.0 GeV MCPs with charge factor $\varepsilon = 10^{-1}$ at zenith angle $\theta = 0°$ simulated with SIBYLL 2.3c (solid lines), SIBYLL 2.3d (dashed lines) and DPMJET III (dotted lines). For comparison, the muon flux is shown for the same models.

Comparing the atmospheric models, neither the muon flux nor the MCP fluxes show any relevant model dependent difference, as can be seen in Fig. 3.22.

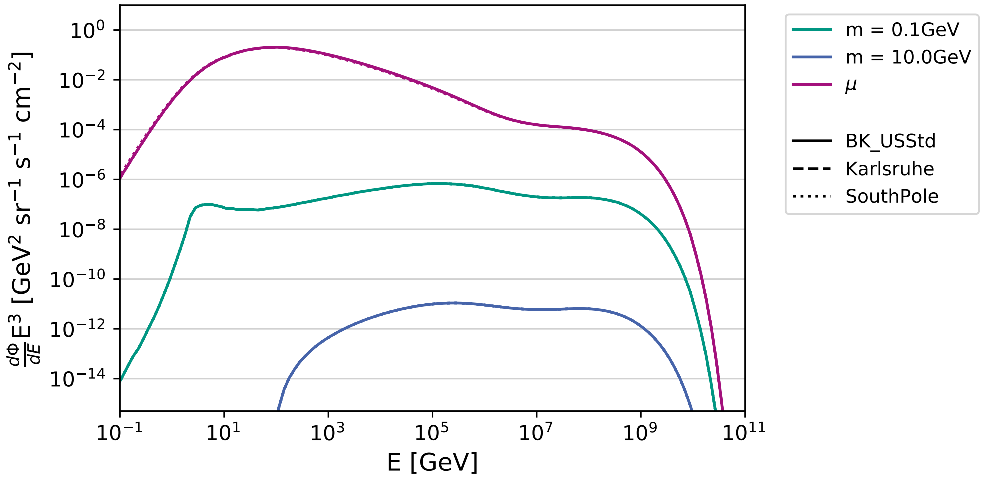

Figure 3.22: Differential flux spectrum for 0.1 GeV and 10.0 GeV MCPs with charge factor $\varepsilon = 10^{-1}$ at zenith angle $\theta = 0°$ simulated with the BK_USStd atmospheric density model (solid lines), an atmospheric model for Karlsruhe (dashed lines) and a model for the atmosphere at the South Pole in August (dotted lines). For comparison, the muon flux is shown for the same models.

Finally, when comparing the primary models Hillas-Gaisser-2012 H3a, H4a [51] and GlobalSplineFitBeta [52] (also see comparison of these and more models in [53]), we find that the models differ mainly for high energies.

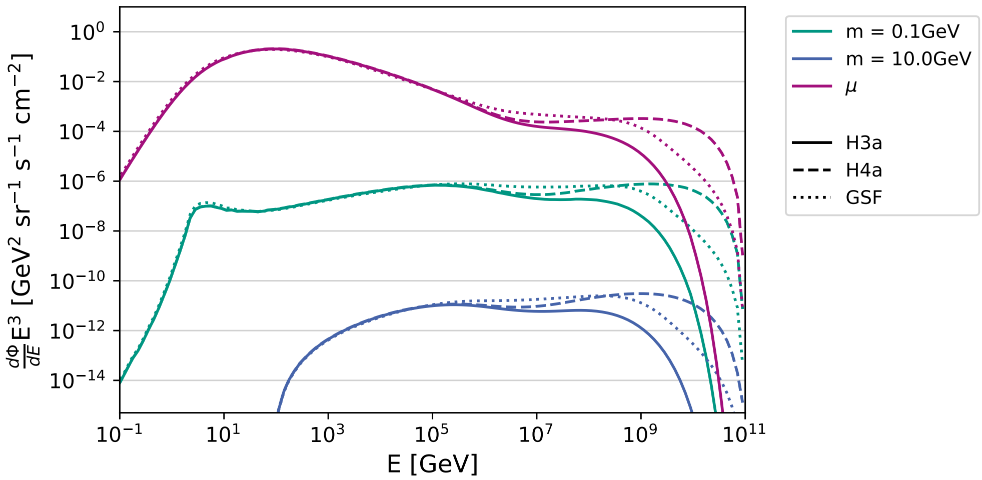

Figure 3.23: Differential flux spectrum for 0.1 GeV and 10.0 GeV MCPs with charge factor $\varepsilon = 10^{-1}$ at zenith angle $\theta = 0°$ simulated with the Hillas-Gaisser-2012 H3a primary model (solid lines), the according H4a model (dashed lines) and the GlobalSplineFitBeta model (dotted lines). For comparison, the muon flux is shown for the same models.

4. Particle Propagation through Earth

To calculate the flux of millicharged particles at a detector location, their propagation through Earth and the resulting energy losses need to be taken into account. In this chapter, we're going to take a look at Earth's geometry and density, as well as the resulting energy losses for MCPs. These results are also going to be used to verify our analysis so far to some extent.

4.1 Earth properties

Fig. 4.1 shows a schematic depiction of Earth with a detector located at depth h. For the calculations in this chapter, we are going to assume $h = 1.4km$, which ist the depth of the *XENON1T* detector.

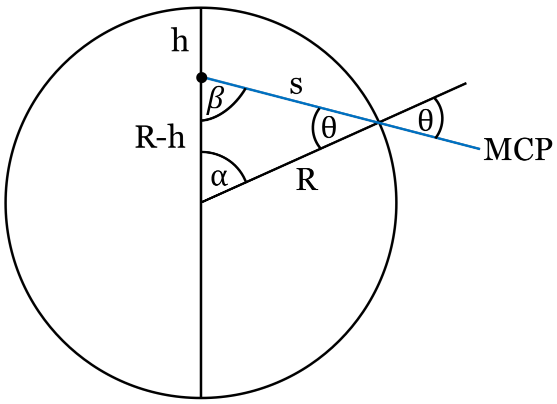

Figure 4.1: Schematic view of Earth with a detector located at depth h. Trajectory of an incoming MCP is shown in blue. The important angles for our calculation are the detector angle β, the zenith angle θ and the angle around the Earth's center α.

An incoming particle (trajectory shown in blue) travels a total distance s through Earth before it reaches the detector location. MCPs that are produced in the atmosphere striking the Earth's surface at zenith angle θ hit the detector at a specific angle β. The according angle around the Earth's center will be noted by α.

The relations between the angles α, β and θ can be determined by the *law of sines* as

$$\frac{R}{\sin\beta} = \frac{R-h}{\sin\theta} = \frac{s}{\sin\alpha} \tag{4.1}$$

Using the *law of cosines*, the relation between s and α and θ can be calculated as

$$\begin{aligned} s^2 &= (R-h)^2 + R^2 - 2\,R\,(R-h)\cos\alpha \\ &= -R\cos\theta + \sqrt{R^2\cos^2\theta - (R-h)^2 + R^2} \end{aligned} \tag{4.2}$$

Fig. 4.2 shows, how α and θ depend on the detector angle β.

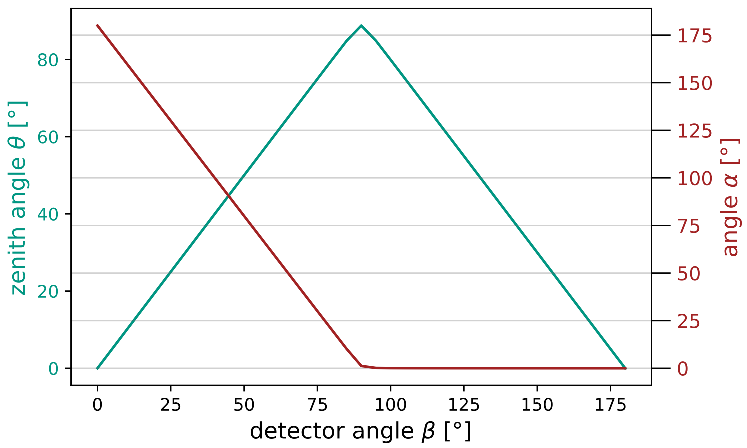

Figure 4.2: Dependence of zenith angle β and angle around the Earth's center α on the detector angle β.

The dependence of the angles α, β and θ on the travel length s is shown in Fig. 4.3.

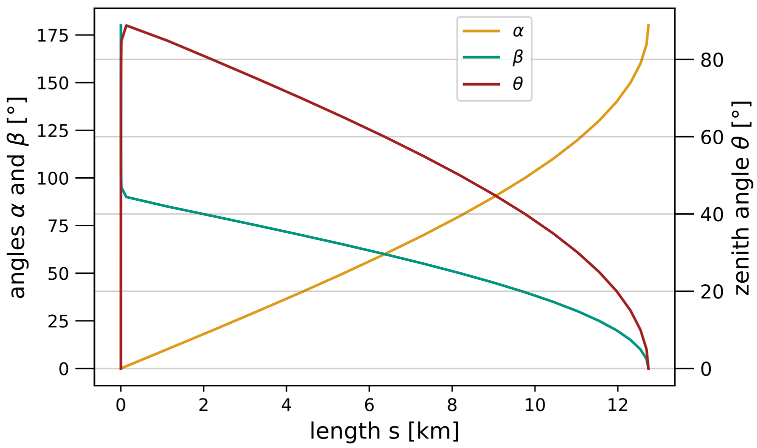

Figure 4.3: Dependence of zenith angles α, β and θ on the travel length s.

Because the Earth consists of various layers of increasing densities from standard rock to its iron core, a detailed model description of these densities needs to be implemented. For this purpose, the Preliminary Reference Earth Model (or PREM for short) by *Dziewonski* and *Anderson* [11] is used in this work to describe the radius-dependent density of the Earth. The complete PREM also includes further properties such as the pressure, temperature or gravity dependence on the planetary radius. It is widely used for geophysical analyses, for example to study the subterranean diffusion of seismic waves.

The parametrization used in this analysis is taken from ref. [54] and defines the density at a given distance r from the Earth's center as

$$\rho(r) = \begin{cases} 13.0885 - 8.8381\,x^2, & r < 1221.5, \\ 12.5815 - 1.2638\,x - 3.6426\,x^2 - 5.5281\,x^3, & 1221.5 < r < 3480, \\ 7.9565 - 6.4761\,x + 5.5283\,x^2 - 3.0807\,x^3, & 3480 < r < 5701, \\ 5.3197 - 1.4836\,x, & 5701 < r < 5771, \\ 11.2494 - 8.0298\,x, & 5771 < r < 5971, \\ 7.1089 - 3.8045\,x, & 5971 < r < 6151, \\ 2.691 + 0.6924\,x, & 6151 < r < 6346.6, \\ 2.9, & 6346.6 < r < 6356, \\ 2.6, & 6356 < r < 6368, \\ 1.02, & r < R_\oplus \end{cases} \tag{4.3}$$

with ρ in units of g/cm^3, r in km, the Earth's radius $R_\oplus = 6371\,\text{km}$ and $x \equiv r/R_\oplus$ being a scaled radial variable.

As can be seen in eq. 4.3, this parametrization of the PREM differentiates between ten different earthly layers. Fig. 4.4 shows these layers as a function of the planetary radius, note that in the more outward regions the layers become rather nuanced and are harder to differentiate. The Earth's inner and outer core are mostly composed of iron and nickel in a solid and fluid state. Their density lies above $\rho = 10\,\text{g/cm}^3$. Above the Core-Mantle-Boundary (CMB), the mantle and crust regions possess densities below $\rho = 6\,\text{g/cm}^3$. The PREM also includes a 3 km layer of ocean water with a density of $\rho \approx 1.0\,\text{g/cm}^3$.

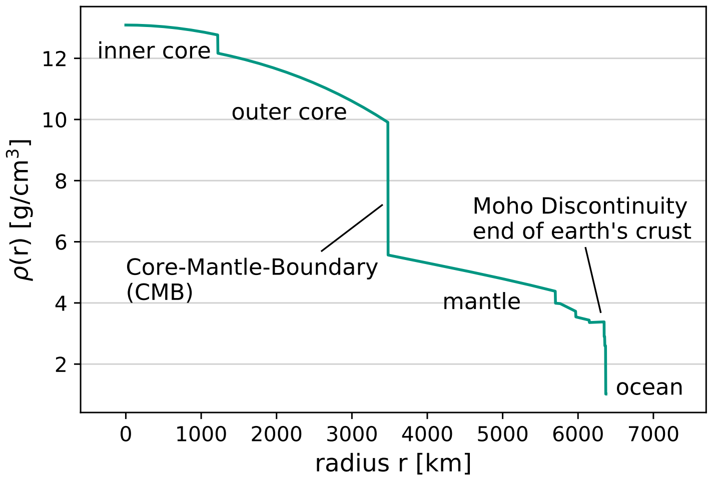

Figure 4.4: Density distribution along planetary radius r as described by the Preliminary Reference Earth Model (PREM)

For MCPs travelling through earth, this means that particles coming from angles $\beta \lessapprox 88.7°$ travel through several such density layers. Since the energy losses in Earth depend strongly on this effect, the local density $\rho(r_{curr})$ depending on the current distance r_{curr} of a moving particle from the Earth's center can be calculated with 4.3 and 4.4. r_{curr} is a function of the distance d the particle has already travelled on it's trajectory s and the detector angle β.

$$r_{curr} = \sqrt{(R-h)^2 + (s(\beta)-d)^2 - 2(R-h)(s(\beta)-d)\cos(\beta)} \tag{4.4}$$

The resulting density distribution as a function of the total travel distance s is shown in Fig. 4.5 for several angles below the threshold of $\sim 88.7°$, above which particles only travel through the outermost layer, which in the PREM is assumed to be 3 km thick.

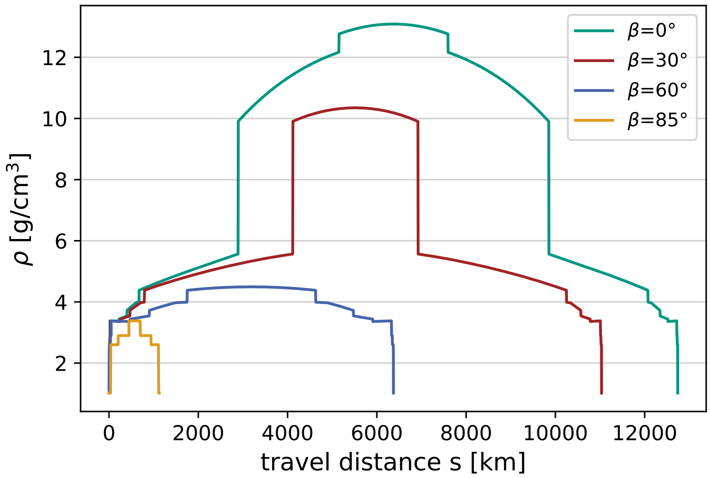

Figure 4.5: Densities along travel distance s for particles reaching the detector from angles $\beta < 88.7°$. Particles reaching the detector from larger anglesβ only traverse through the outermost planetary layer, because their trajectory never leaves the region of 3 km underneath the Earth's surface.

4.2 Energy loss of MCPs on trajectory through the Earth

When travelling through the Earth, particles lose a substantial amount of energy through ionization and radiative energy losses. The energy loss of MCPs in matter has already been determined in section 3.6 as

$$-\left\langle \frac{dE}{dX} \right\rangle = a(E) + b(E)E \tag{4.5}$$

The same parameters chosen for $a(E)$ and $b(E)$ are going to be used for this analysis, just this time we are going to calculate the total energy loss ourself instead of having MCEq do it for us. With the densities determined in the previous chapter, the total energy loss can be calculated for each particle mass, zenith angle and charge factor ε as

$$\left(\frac{dE}{dX}\right)_{curr} = -\left\langle \frac{dE}{dX} \right\rangle \cdot \rho_{(PREM)}(r_{curr}) \cdot dX \tag{4.6}$$

with a stepwise computation of the energy loss with step size dX. The step size dX is chosen to be 100 m for angles $\beta > 100°$ and 1 km otherwise. For each step, r_{curr} and the according density $\rho_{(PREM)}(r_{curr})$ are being calculated and the energy losses can be added up such as

$$\left(\frac{dE}{dX}\right)_{tot} = \sum_{0}^{s(\beta)} \left\langle \frac{dE}{dX} \right\rangle \cdot \rho_{(PREM)}(r_{curr}) \cdot dX \tag{4.7}$$

For MCPs with mass 10 GeV and charge factor $\varepsilon = 10^{-1}$ as well as muons, the total energy losses $\left(\frac{dE}{dX}\right)_{tot}$ are shown in Fig. 4.6 for several angles.

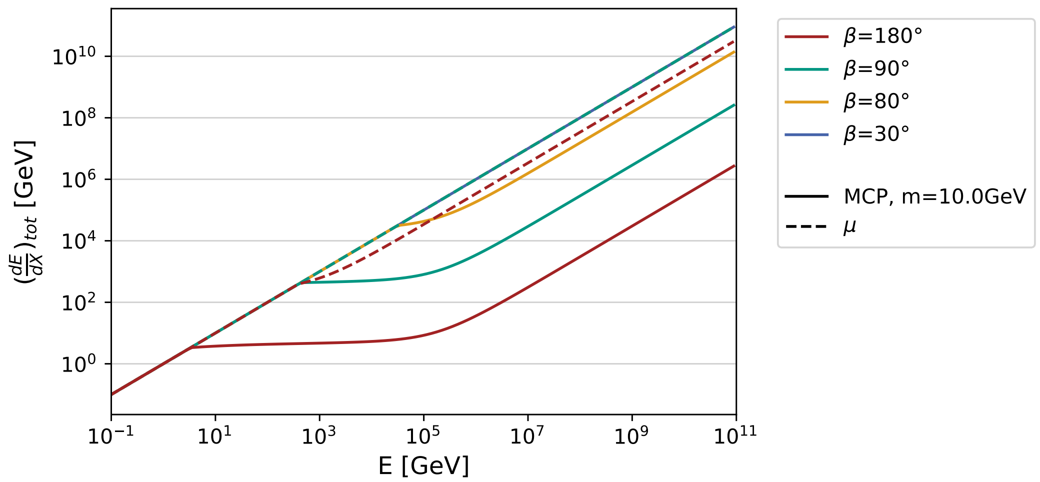

Figure 4.6: Total energy loss of MCPs with a mass of 10 GeV and charge factor $\varepsilon = 10^{-1}$ (solid lines) and muons (dashed lines). The muon energy loss is visibly high even at the largest angles, because their charge is of course not diminished by a factor ε.

The energy losses become larger at smaller angles, where a longer distance through Earth has to be covered by the incoming particles. The energy losses reach their maximum at the primordial energy of the respective particle, which can be seen as a diagonal in this graph. Note that muons lose energy much faster, because their charge is not reduced by a factor ε.

The dependence of the energy losses for MCPs at a detector angle of $\beta = 80°$ is depicted in Fig. 4.7 for various charges and masses. MCPs with a lower charge lose less energy in matter, whereas particles with a lower mass lose their energy faster.

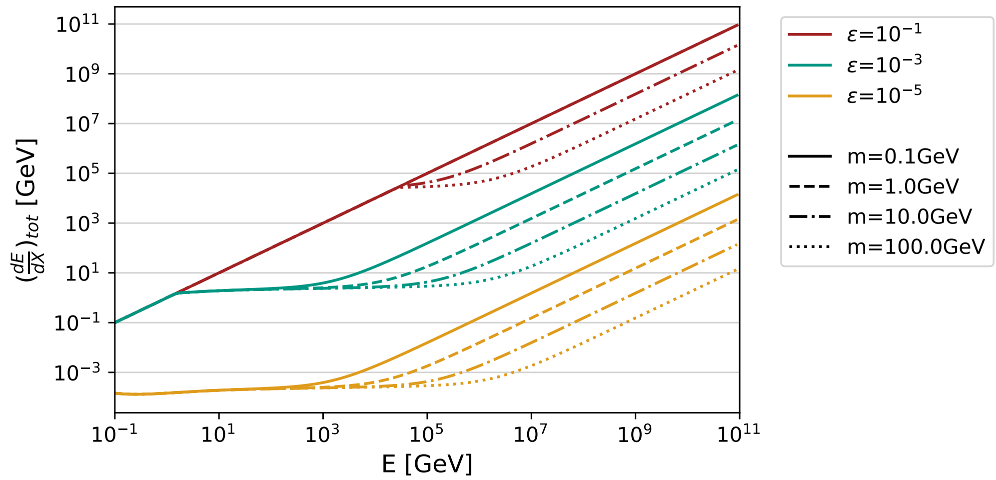

Figure 4.7: Total energy loss of MCPs at a detector angle of $\beta = 80°$ shown for charge factors $\varepsilon = 10^{-1}$, 10^{-3} and 10^{-5} as well as masses $m = 0.1\,\text{GeV}$, $1.0\,\text{GeV}$, $10.0\,\text{GeV}$ and $100.0\,\text{GeV}$.

The general shape of the energy loss functions above is reminiscent of the form of the mass stopping power in matter as also seen in Fig. 3.15, though of course the total energy losses depend on the described density model and MCP parameters.

4.3 Particle Flux at the Detector

The interesting quantity here is of course the particle flux at a detector location. This can be achieved by observing the effect of the energy losses in matter described in the previous chapter on the particle fluxes at sea level determined in chapter 3.7. For each particle, the detector energy E_{det} can be easily determined from the energy at the Earth's surface E_{surf} as

$$E_{det} = E_{surf} - \left(\frac{dE}{dX}\right)_{tot} \tag{4.8}$$

The resulting detector energy E_{det} can be seen in Fig. 4.8. MCPs with lower charges lose less energy and seem to be retaining almost their entire surface energy. Light MCPs lose their energy faster. Comparing the red curves in Fig. 4.8 to the red curves in Fig. 4.7, the effect of the total energy loss reaching its maximum becomes obvious: Only MCPs of masses $m = 10.0\,\text{GeV}$ and $100.0\,\text{GeV}$ with $\varepsilon = 10^{-1}$ do not lose all of their energy, and are therefore still present in Fig. 4.8.

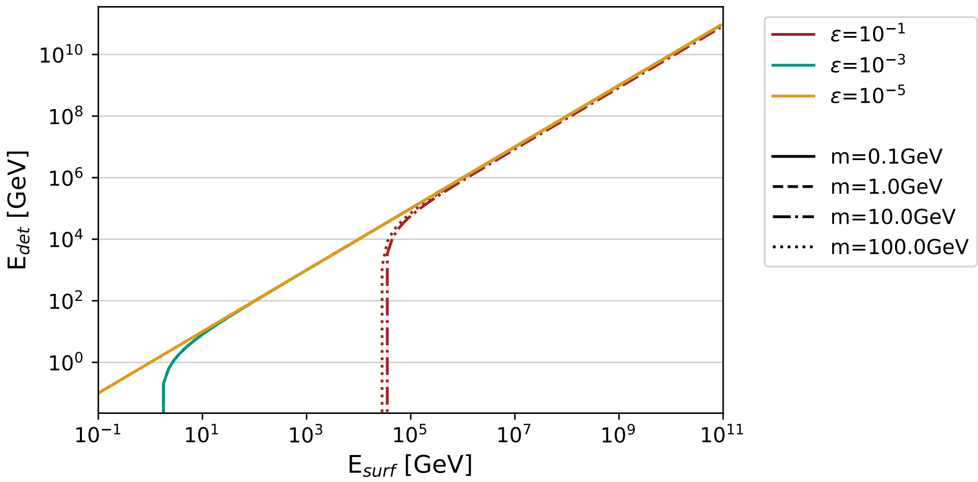

Figure 4.8: Detector energies for MCPs with charge factors $\varepsilon = 10^{-1}$, 10^{-3} and 10^{-5} as well as masses $m = 0.1\,\mathrm{GeV}$, $1.0\,\mathrm{GeV}$, $10.0\,\mathrm{GeV}$ and $100.0\,\mathrm{GeV}$ as a function of their corresponding surface energy E_{surf}.

The particle flux at the detector location is now calculated by integrating over all detector energies. For each detector energy, the corresponding surface energy can be taken from Fig. 4.8. The according flux of the surface particle energy is equivalent to the resulting flux at the detector. This operation can be simply expressed as

$$\frac{d\Phi}{dE_{det}}(d\beta\, dA\, dt\, dE) = \frac{d\Phi}{dE_{surf}}(d\theta(\beta)\, dA\, dt\, dE_{det}) \tag{4.9}$$

and for the computation results in two simple interpolations as shown in the following code example for muons:

```
E_new = e_grid - dEdX_tot_inv # shape (37,121)
for b_idx in range(len(betas)): # len(betas) = 37
    for e_idx, e_det in enumerate(e_grid):
        e_surf = np.interp(e_det, E_new[b_idx], e_grid)
        phi_det_mu[b_idx][e_idx] = np.interp(e_surf,
                                   e_grid, phi_surf_mu[b_idx])
```

The first interpolation in this example determines the corresponding surface energy for each detector energy. The second interpolation interlinks the respective muon fluxes.

To be able to make comparative analyses, the muon flux is an important quantity. Fig. 4.9 displays the muon flux for different angles $\beta > 90°$. Below this angle, the earth is not transparent for any muons and the flux is expected to become zero. The intensity of this resulting muon flux at the detector will be used again in section 4.4.

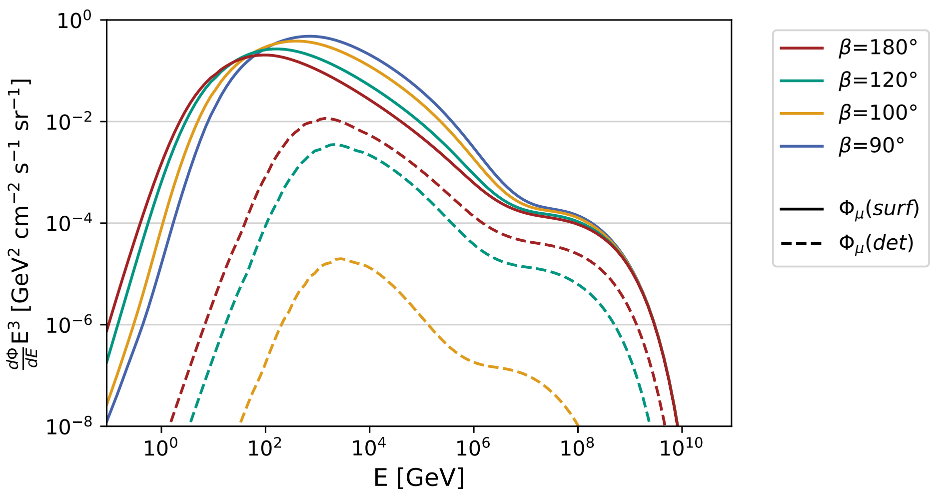

Figure 4.9: Muon flux for different angles $\beta > 90°$ at sea level (solid lines) and at the detector (dashed lines).

The resulting MCP fluxes at the detector depth, still assuming $h = 1.4km$, depend strongly on the MCP mass, charge and arrival direction. For reasons of clarity and comprehensibility, these dependencies are displayed in the following three figures rather than showing them all together. The underlying constants are chosen for presentation purposes, so they differ in each plot and are noted in the respective captions. Another conspicuity that should be noted is the apparent increase of the detector flux compared to the flux at sea level in some plots, especially at higher energies. This is an artefact of the simplicity of the interpolation method decribed above and becomes even more visible due to the multiplication of the flux with E^3. Having said that, these anomalies are always of minor orders of magnitude and insignificant.

The angular dependency of the MCP flux at the detector on the detector angle β is shown in Fig. 4.10 for MCPs with a mass of 0.1 GeV and charge factor $\varepsilon = 10^{-2}$. Unsurprisingly, the flux decreases with the angle β, because the travel distance s through the Earth increases and so does the total energy loss.

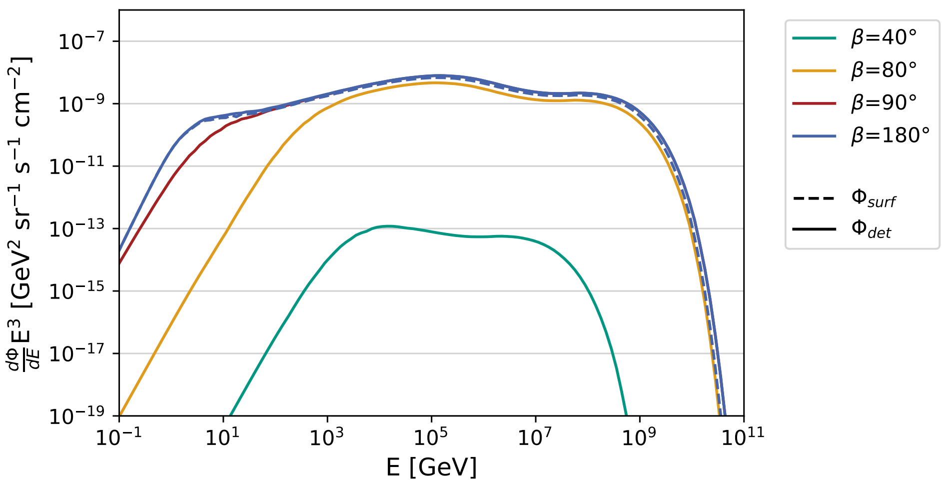

Figure 4.10: The MCP flux at the detector depends on the detector angle β. The detector flux is shown for MCPs with a mass of 0.1 GeV and charge factor $\varepsilon = 10^{-2}$ at different angles β.

Fig. 4.11 shows the dependency of the detector particle flux of the particle mass for MCPs with a charge factor $\varepsilon = 10^{-2}$ reaching the detector at an angle $\beta = 60°$. The energy losses for lighter particles are higher, as already seen in Fig. 4.7. The increase of Φ_{det} compared to Φ_{surf} does not originate in the interpolation issue. Instead, it is an expected effect from higher energy particles arriving at the detector at lower energies.

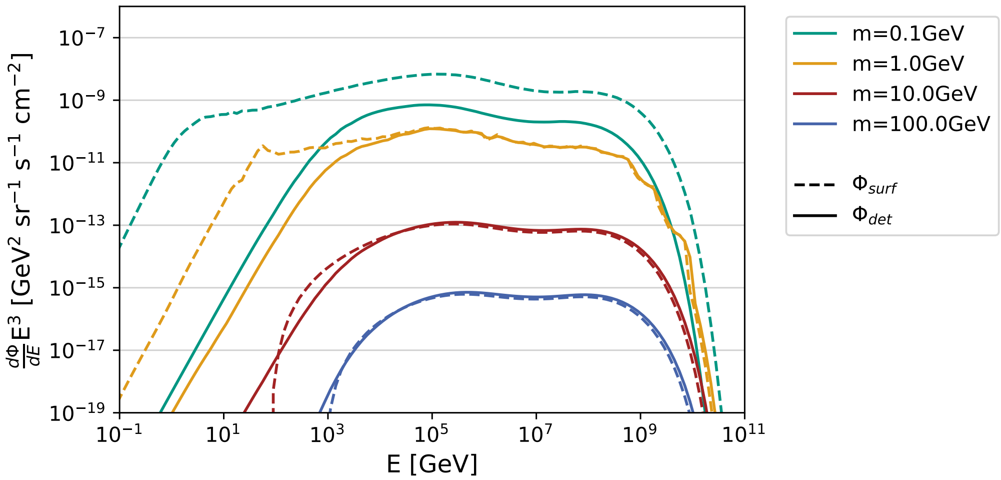

Figure 4.11: Dependency of the detector particle flux on the particle mass for MCPs with a charge factor $\varepsilon = 10^{-2}$ and detector angle $\beta = 60°$.

Finally, the detector flux also depends on the MCP charge diminishing factor ε as shown in Fig. 4.12 for MCPs of mass 0.1 GeV and detector angle $\beta = 90°$. Particles with lower charges become more and more neutrino-like and interact less and less with matter, causing them to lose energy to a lesser extent and therefore show a smaller to nonexistent decrease in the particle flux.

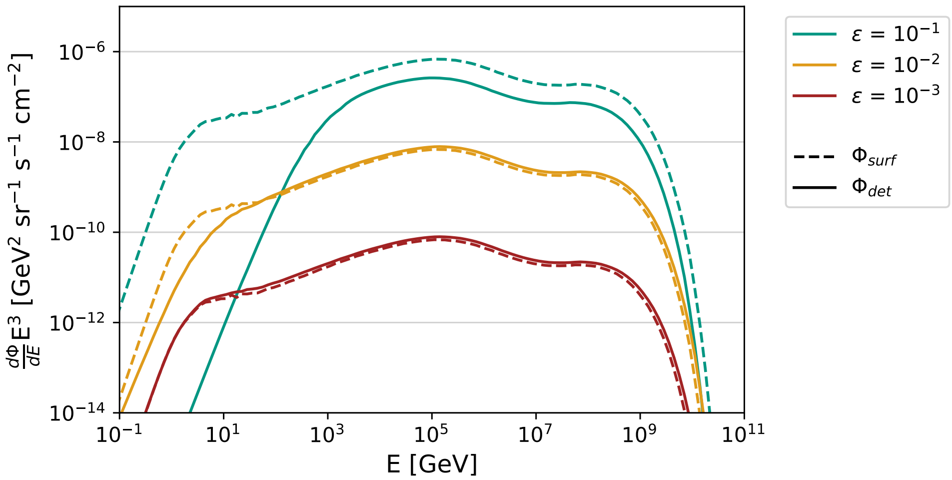

Figure 4.12: The MCP flux at the detector depends on the MCP charge diminishing factor ε shown for MCPs of mass 0.1 GeV and detector angle $\beta = 90°$.

These or similar particle fluxes have been calculated before in other ways, so to improve the reliability of our results, in the next chapter we are going to take a look at how the fluxes shown above compare to other results.

4.4 Modelling Uncertainties

The muon flux is a widely studied figure in astroparticle physics. To cross check and evaluate the analysis so far, a comparison of both the muon flux at sea level as well as the muon intensity underground will be made with data taken from ref. [55].

First, when comparing the muon flux at sea level with Fig. 4a and b from ref. [55] as shown in Fig. 4.13, the conservative nature of the simulation with MCEq becomes visible. The data points have been taken from ref. [55] and the scales have been converted from muon momentum to kinetic energy as we are accustomed to with

$$E_{kin,\mu} = \sqrt{p_\mu^2 + m_\mu^2} - m_\mu \tag{4.10}$$

Though the muon flux differs from the data, note that the y-scale is linear and the deviations are rather small. The muon flux is shown for the Hillas-Gaisser-2012 H3a [51] and the GlobalSplineFitBeta [52] models, since these models showed the largest deviations in section 3.8. The difference of the muon flux remains small and cannot make up for the difference to the data points.

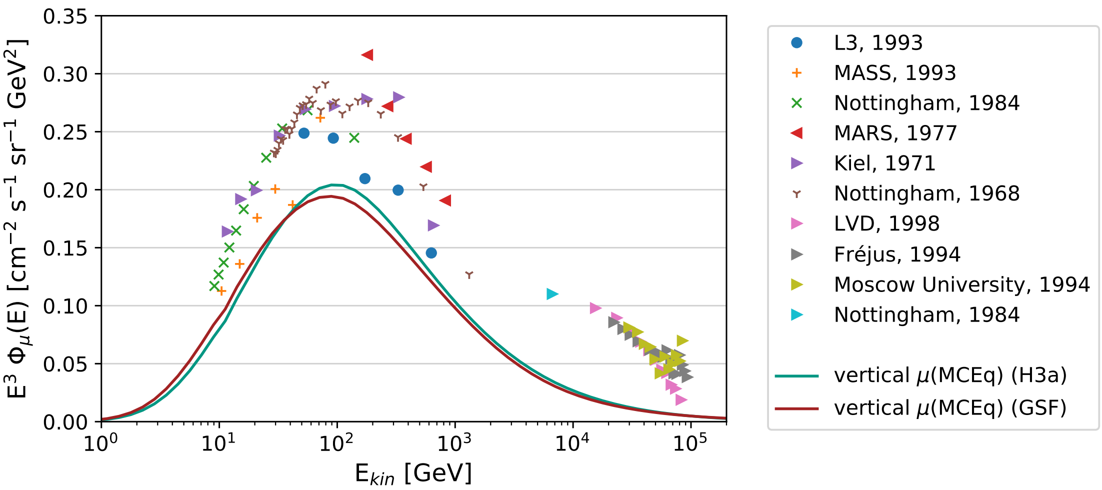

Figure 4.13: The vertical muon flux at sea level as simulated by MCEq is shown as a solid line. The data points are taken from [55] and references therein.

Fig. 4.14 is taken from Fig. 6 in [55] and shows the intensity of the muon flux as a function of the depth in km w e as measured by various experiments. The calculated muon intensity for our analysis is shown in green and with higher energies becomes visibly lower than the measured data, at higher depths it differs with 2 or 3 magnitudes. As seen in Fig. 4.13, the muon flux simulated by MCEq is already lower than the actual data, which of course contributes to a lower flux and therefore intensity underground. This effect might also be due to the simple approximation we made for the radiative energy loss factor b in sec. 3.6. In addition, the used Earth density model might be underestimating the Earth density for the shown depths. Nonetheless our analysis remains conservative as the muon intensity does not exceed the expected values.

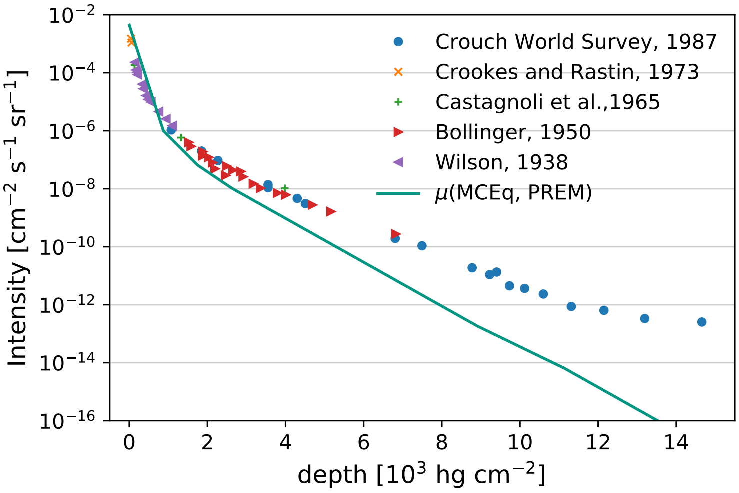

Figure 4.14: Muon intensity per km.w.e. depth shown for our analysis (green line) compared to data from various experiments. Data taken from [55], respective publications for data: [56] [57] [58] [59] [60].

For millicharged particles, a comparison of the detector flux as a function of the zenith angle θ can be made with Fig. 4.15 (Fig.6 in ref. [9]). The MCP flux is calculated for a MCP mass of 10 MeV at particle energies $E = 1.0GeV$ and $E = 5.0GeV$ at the $Super-Kamiokande$ detector, that is $\sim 1\,\text{km}$ deep underground.

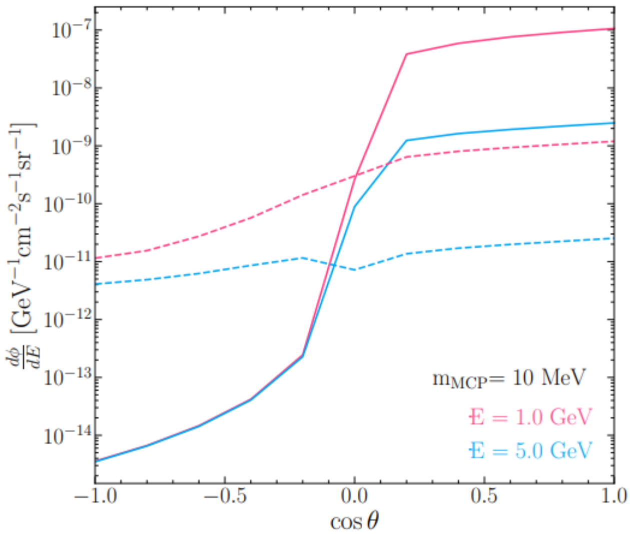

Figure 4.15: MCP flux calculated in [9] for a MCP mass of 10 MeV at particle energies $E = 1.0\,\text{GeV}$ and $E = 5.0\,\text{GeV}$ at a depth of $\sim 1\,\text{km}$. Solid lines show MCPs with a charge factor of $\varepsilon = 10^{-1}$, $\varepsilon = 10^{-2}$ MCPs are shown in dashed lines.

The lowest particle mass in our analysis is 100 MeV, so Fig. 4.16 shows the particle flux for the same parameters, but for MCPs of masses 100 MeV and 1.0 GeV.

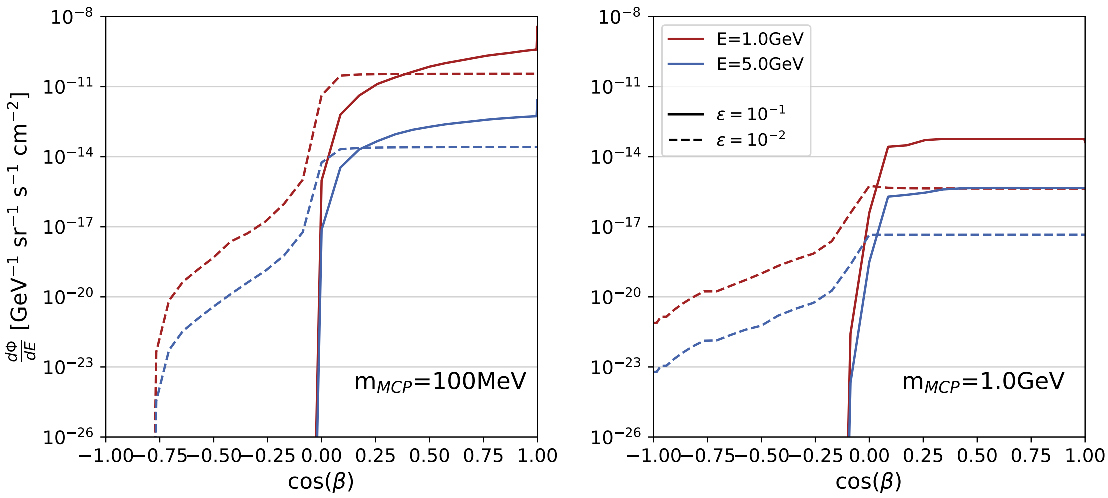

Figure 4.16: MCP flux as a function of the zenith angle θ for MCPs. Properties are all the same as seen in Fig. 4.15

As a takeaway from this comparison, the shape and magnitude of our calculated results behave as expected.

5. Detector Signal and New Constraints

With the particle flux at an underground detector location determined in the previous chapter, the last step is now to recreate the expected signal in a designated detector before final constraints can be achieved by comparing the calculated expected signal to real detector data. In this work, the detectors *XENON1T* and *Super-Kamiokande* were used to determine constraints in the MCP mass- and charge-space. They will be briefly presented, though the main focus lies on extracting the significant properties for the analysis. Through this study, new limits for MCPs have been found and will be presented at the end of this chapter.

5.1 Detector Signal through electron recoils

A lepton-like particle will interact with matter inside a detector volume through electron scattering, producing recoil electrons that can be recorded by various detectors. Experiments that function on electron recoils will often count the number of recoil events happening per unit time, fiducial target mass and recoil energy.

Usually, the electrons in the target volume are assumed to be free, because for high energy transfers, the binding energy of an electron to a nucleus becomes negligible. This approximation has also been used in this analysis, though a study on the effect of this simplification can be found in [61] and it should be noted that a further enhancement of our results could come from implementing the *Relativistic Impulse Approximation.*

The differential cross section for a MCP with mass m_{MCP} and total energy $E_{MCP} = E_{kin} + m_{MCP}$ to scatter off an electron can be written as

$$\frac{d\sigma}{dE_r} = \pi\alpha^2\varepsilon^2 \, \frac{2E_{MCP}^2 m_e + E_r^2 m_e - E_r(m_{MCP}^2 + m_e(2E_{MCP} + m_e))}{E_r^2 m_e^2 (E_{MCP}^2 - m_{MCP}^2)} \tag{5.1}$$

as also used in ref. [10]. Here, m_e is the electron mass $m_e \approx 511\,\text{keV}$, α is the electromagnetic Feinstruktur constant $\alpha \approx \frac{1}{137}$, ε is the MCP charge factor and E_r is the recoil energy.

An approximation in the ultrarelativistic limit is also given in ref. [10] as

$$\left.\frac{d\sigma}{dE_r}\right|_{E_{MCP} \gg m_{MCP}, m_e, E_r} \cong \frac{2\pi\alpha^2\varepsilon^2}{E_r^2 m_e}. \tag{5.2}$$

For MCP masses of $m = 10.0\,\text{GeV}$, the differential cross section is shown as a function of the electron recoil energy in Fig. 5.1.

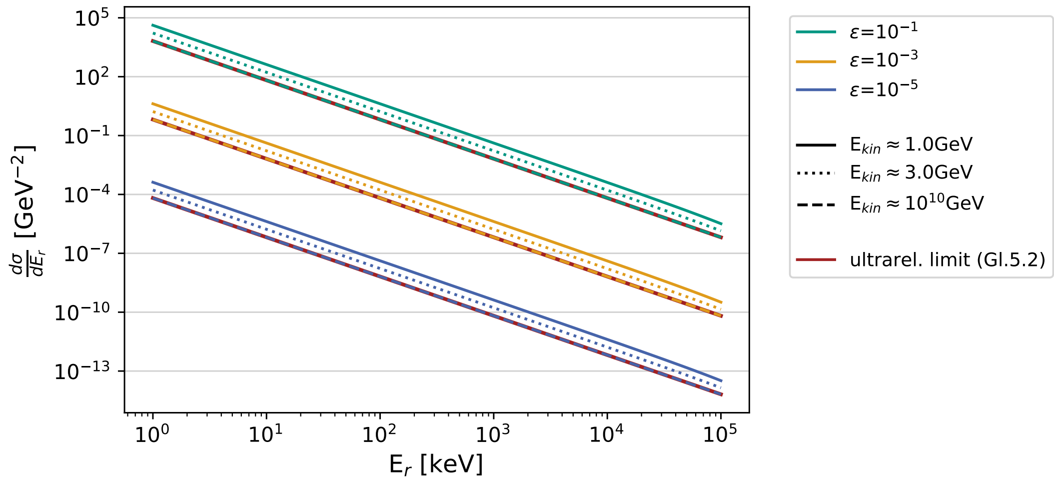

Figure 5.1: Differential electron recoil cross section shown for MCPs with mass 10.0 GeV for different charge factors ε and MCP energies E_{MCP}. The cross section for the ultra-relatvistic limit as described in eq. 5.2 is shown in red.

The differential event rate for each recoil energy E_r expected from the MCP flux $\Phi(\beta)_{det}$at a detector angle β can be received by an integration over all considered MCP energies as

$$\frac{dN}{dE_r d\beta} = n_e \int dE_{MCP} \frac{d\Phi(\beta)_{det}}{dE_{MCP} d\beta} \frac{d\sigma}{dE_r}, \tag{5.3}$$

where n_e is the number of electrons in the fiducial target volume [9].

Finally, the differential event rate N for each E_r bin can be obtained by summing over all detector angles β and multiplying with the total time exposure t_{det} and the E_r-dependent detector efficiency $\epsilon_{eff}(E_r)$ as

$$\frac{dN}{dE_r} = t_{det}\, \epsilon_{eff}(E_r) \sum_{0°}^{180°} d\beta \sin(\beta)\, \Delta(\beta)\, \frac{dN}{dE_r d\beta}. \tag{5.4}$$

Several of the parameters used in the above calculation are detector dependent, so the following chapter will give a brief overview over the two detectors used in this analysis.

5.2 Detector Properties

5.2.1 XENON1T

The XENON experiment is an underground detector designated to search for dark matter particles. It has been designed to be able to detect weakly interacting massive particles (WIMPs), but because of its incredibly low backround rates, large target mass and low energy threshold, the XENON1T detector also is a promising experiment for other sorts of dark matter such as solar axions or bosonic dark matter [12]. These properties make XENON1T interesting for this work as well. The detector has a fiducial volume of 1000 kg of liquid Xenon in a time projection chamber (LXe TPC) and is located at a depth of 1.4 km at the Laboratori Nazionali del Gran Sasso (LNGS). The construction of the detector can be seen in Fig. 5.2.

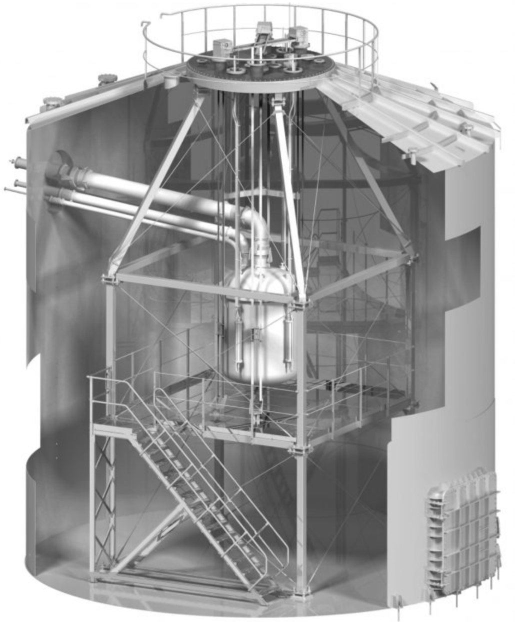

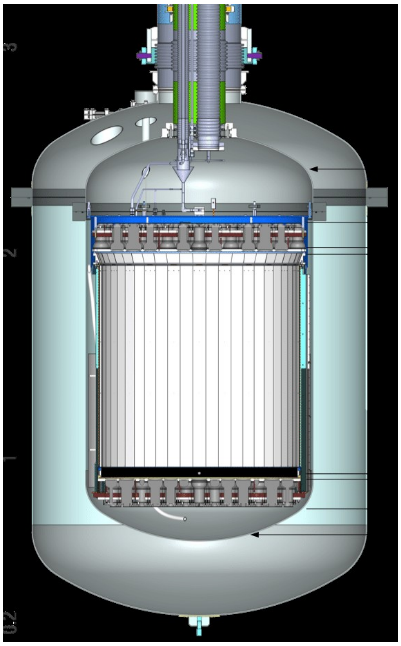

Figure 5.2: View of the outer and inner architecture of the XENON1T detector. Images taken from [62] and [63].

For our purposes, we are interested in the total number of electrons in XENON1T $n_e(Xe)$, the detector efficiency $\epsilon_{eff}(E_r)$, the range of electron recoils of interest for a set of actual data taken in a time interval t_{det} and the background at this energy range. The number of electrons in the XENON1T fiducial volume calculates to

$$n_e(Xe) = Z_{Xe} \cdot \frac{m_{fid}}{m_{Xe} \cdot 1.66 \cdot 10^{-27}} \approx 2.48 \cdot 10^{29} \tag{5.5}$$

with the atomic number of Xenon $Z_{Xe} = 54$, fiducial mass $m_{fid} = 1000\,\mathrm{kg}$ and the atomic mass of Xenon $m_{Xe} = 131.29\,\mathrm{u}$.

The detector efficiency depends on the detection energy and has been taken from Fig. 5.3.

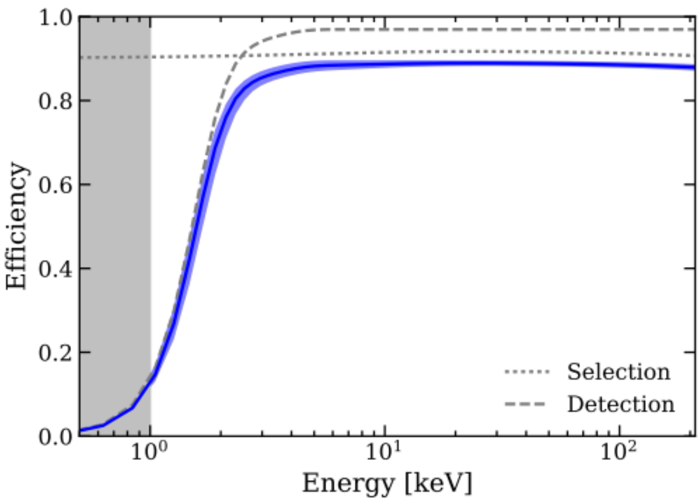

Figure 5.3: Detector Efficiency for XENON1T (blue curve), taken from [64].

The recoil energy region of interest can be taken from Fig. 5.4. This results in a total of 29 energy bins between 1 keV and 30 keV.

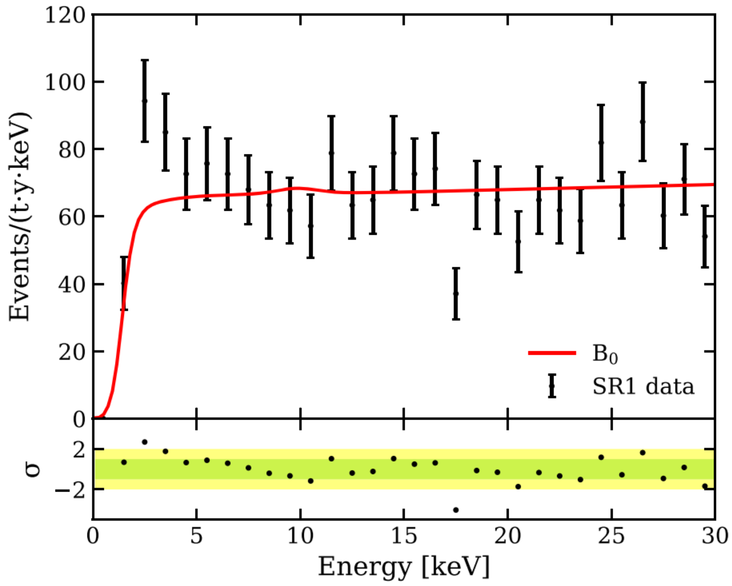

Figure 5.4: Events in XENON1T per tonne, year and keV shown for low electron recoil energies. The red line shows the background signal. Image taken from [64].

The detection time t_{det} for the data shown above is 1 yr, which is equivalent to $365 \cdot 24 \cdot 60 \cdot 60$s for our purposes. These parameters for the XENON1T detector can be simply inserted in eq. 5.3 and eq. 5.4 to obtain the total number of events expected from our simulated MCP fluxes. The results are shown in section 5.3.

5.2.2 Super-Kamiokande

The Super-Kamiokande detector (SK) is a neutrino experiment located at a depth of 1000 m in the Kamioka mine in Japan. The large water tank can be seen in Fig. 5.5. It is around 40 m in diameter and height and holds 50 kt of water, with a fiducial volume of 22.5 kt [65].

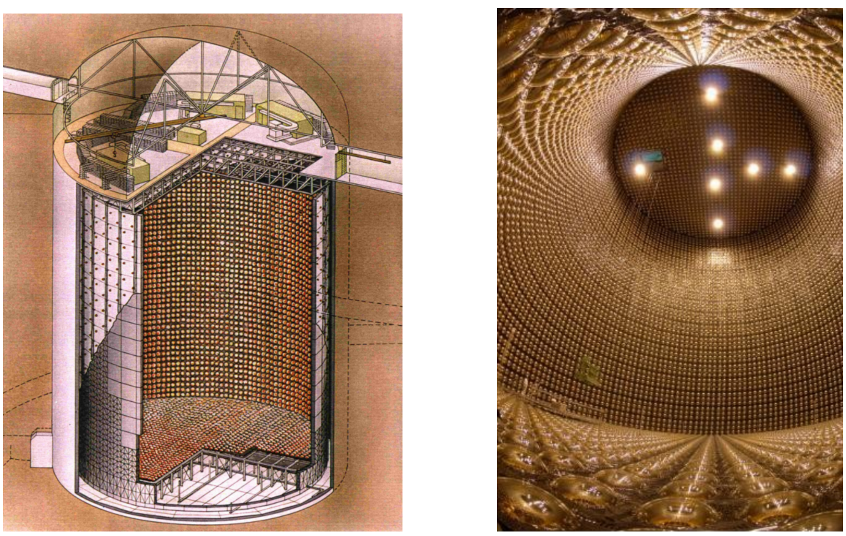

Figure 5.5: View of the outer and inner structure of the Super-Kamiokande detector. Images taken from [66].

The number of electrons in the fiducial volume $m_{fid} = 22.5\,\mathrm{kt}$ can be calculated to

$$n_e(SK) = Z_{H_2O} \cdot \frac{m_{fid}}{m_{H_2O} \cdot 1.66 \cdot 10^{-27}} \approx 7.52 \cdot 10^{33} \tag{5.6}$$

with the number of electrons per water molecule $Z_{H_2O} = 10$ and molecular mass of water $m_{H_2O} = 18.015\,\mathrm{u}$.

The detector efficiency has been taken from [13] and is shown in Fig. 5.6, the data used for our analysis is shown in Fig. 5.7.

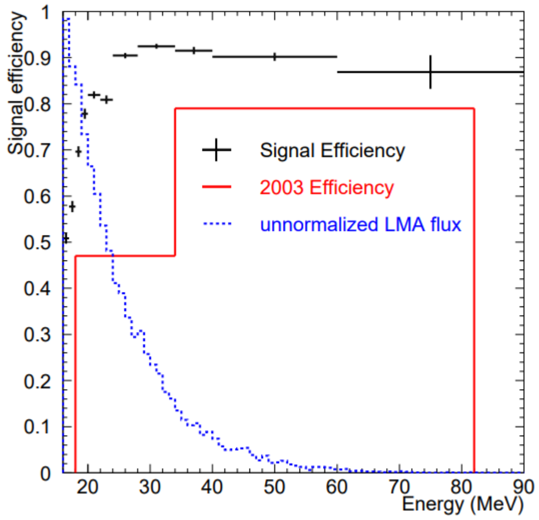

Figure 5.6: Detector Efficiency for Super-Kamiokande (black data points) taken from [13].

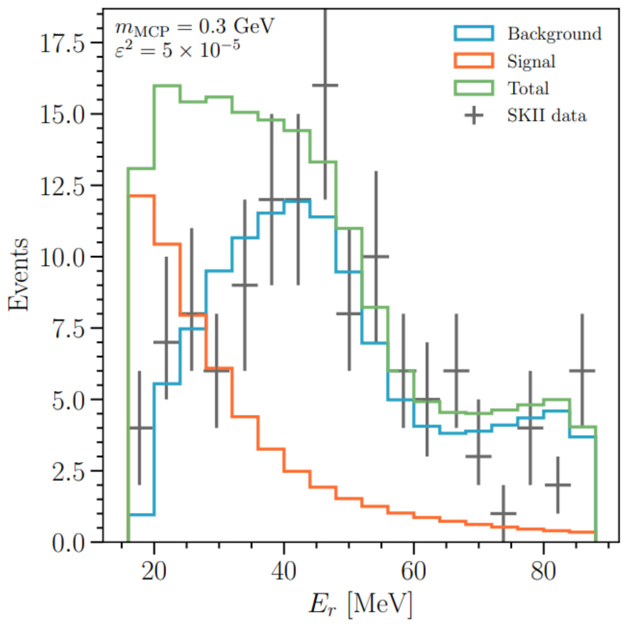

Figure 5.7: Super-Kamiokande data at low recoil energies (black dots) and background (blue line). Image taken from [9].

The range of electron recoil energies of interest lies between 15 MeV and 90 MeV as can be seen in Fig. 5.7. The exposure time for the data shown in Fig. 5.7 is also $t_{det} = 1\,\mathrm{yr} = 365 \cdot 24 \cdot 60 \cdot 60\mathrm{s}$.

5.3 Constraints on MCPs through Detector Signal

With the parameters obtained from the two detectors as described in the last chapter, we can now obtain the expected number of recoil events in the regions of interest for both setups. Since this process is the same for both evaluations, the process is going to be shown exemplary for the XENON1T detector, the results are going to be shown for both analyses at the end of this chapter.

The results of eq. 5.3 and eq. 5.4 are shown in Fig. 5.8 for MCPs with charge factors $\varepsilon = 10^{-1}$ for an exemplary small mass range. The data points (black) and background signal (red line) are taken from Fig. 5.4.

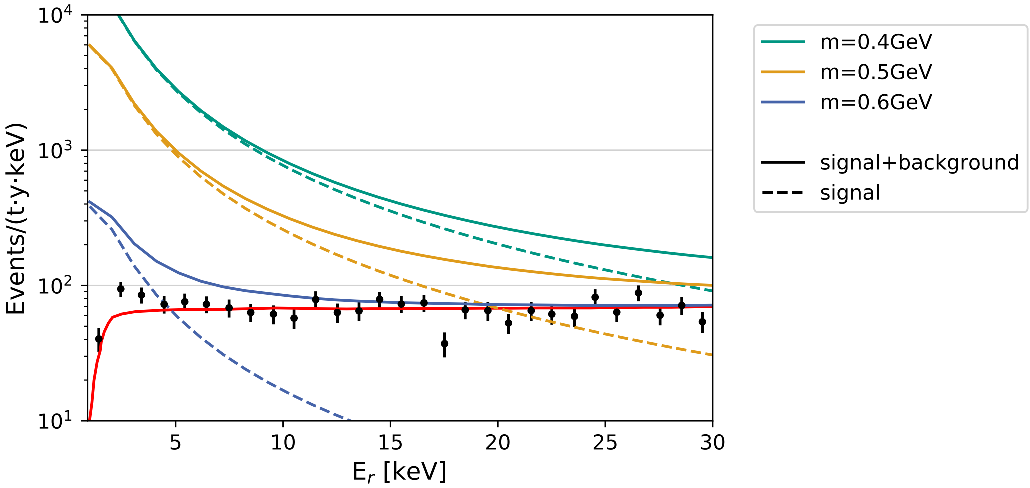

Figure 5.8: Black data points and red background signal are taken from Fig. 5.4. MCP expected detector signal is shown for MCPs with $\varepsilon = 10^{-1}$ and masses 0.3 GeV, 0.4 GeV and 0.5 GeV. Dashed lines show the calculated MCP signal, solid lines show the signal with added background.

To obtain constraints in the MCP charge and mass plane, the results shown above are now compared to the detector data points using a bootstrap analysis.

The signals shown in Fig. 5.8 have been calculated for each implemented MCP mass from 0.1 GeV to 100.0 GeV and a number of 51 ε-factors in the range of 10^0 to 10^{-5}.

The according bootstrap test statistic can be calculated for every mass and ε as shown in [67] with

$$ts = \Delta^T V^{-1} \Delta \tag{5.7}$$

with

$$\Delta = \begin{pmatrix} y_{data,1} - y_{back,1} \\ ... \\ y_{data,n} - y_{back,n} \end{pmatrix} \qquad and \qquad V = \mathbb{1} \begin{pmatrix} \sigma_1^2 \\ ... \\ \sigma_n^2 \end{pmatrix}. \tag{5.8}$$

Here, n is the number of E_r bins equal to the degrees of freedom, y_{data} is a test statistic data set made from a gaussean distribution along the error bars of each of the black data points seen in Fig. 5.8, y_{back} is the according background signal (red line in Fig. 5.8) and σ being the respective errors on the data points. To investigate if the covariance matrix V needs more than just the diagonal elements, i.e. if systematic errors need to be taken into account, a pull-distribution of Δ/σ revealed a gaussean distribution as seen in Fig. 5.9.

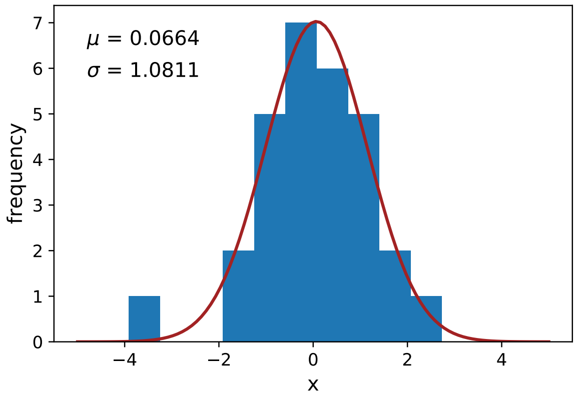

Figure 5.9: Pull distribution shown for Δ/σ. The mean of $\mu = 0.066 \approx 0$ and the $\sigma = 1.0811 \approx 1$ belong to a gaussean distribution, as also shown in the red fit line.

In conclusion, the errors in the XENON1T data are dominated by statistical errors and the covariance matrix V only needs diagonal elements. Adding further σ elements would not bring any improvement to this analysis.

From the test statistic, we can take a cut value of $ts_{cut} \approx 95.53$ for a confidence level of 90%.

The test statistic distribution for each ε as a function of the MCP mass is calculated with $\Delta = y_{signal} - y_{data}$. Here, y_{signal} is the calculated MCP detector signal and y_{data} is the XENON1T data points. The results for various ε can be seen in Fig. 5.10.

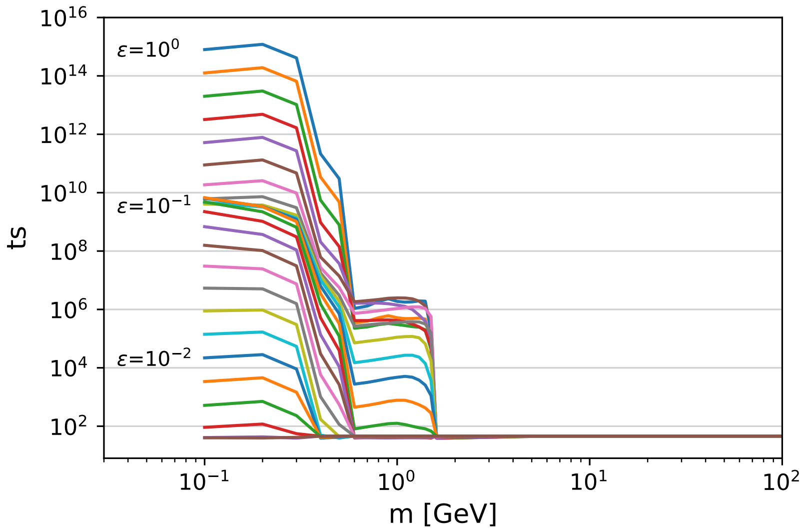

Figure 5.10: Plots for various ε shown as a function of m_{MCP}. The dark blue curves belong to the displayed ε values. Below a value of $\varepsilon = 10^{-2.3}$, no other graphs exceed the detector background.

When turning this plot around, i.e. plotting the statistics for various mass values over ε, we obtain Fig. 5.11. Shown in dark blue is the confidence level of 90% for a cut value of ~ 95.53.

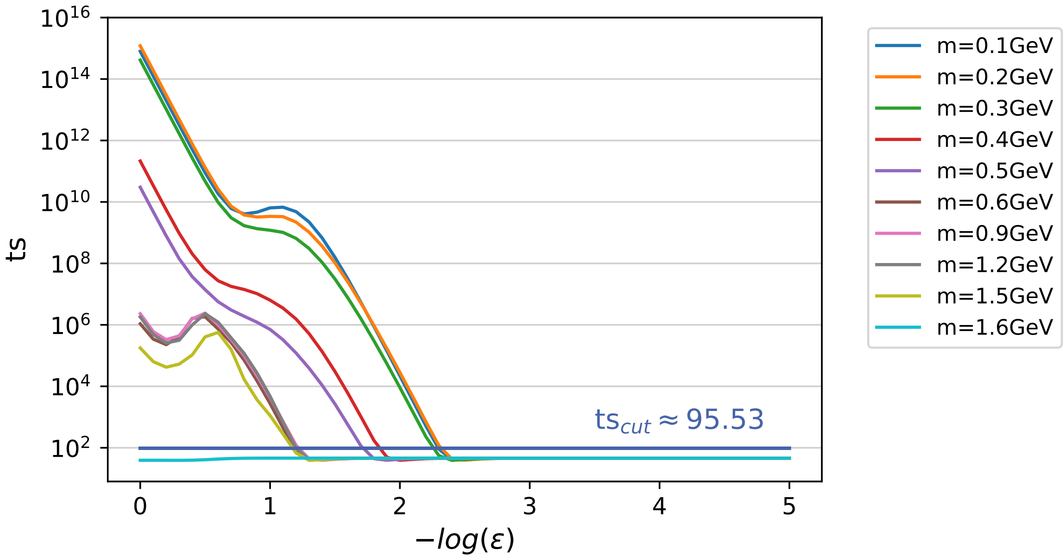

Figure 5.11: Plots shown for various masses (unevenly distributed, see legend) as a function of $-log(\varepsilon)$. The regions where MCPs are produced from J/Ψ-vector meson decay vs. lighter meson decays become visible as the χ^2 for masses $m > 0.5$ GeV, 0.5 GeV $\geq m > 0.3$ GeV and $m \leq 0.3$ GeV form cluster like regions. Also, the "wiggle "seen for higher masses is due to the excess events found at low recoil energies in XENON1T.

By calculating the respective ε-values for each MCP mass m at the 90% confidence level, we receive constraints on MCPs in the mass and charge plane shown in Fig. 5.12. Shown in red are the constraints made by the analysis with XENON1T.

The calculation has been made in the same way for Super-Kamiokande, the resulting constraints are shown in blue.

We have been able to find constraints in the parameter space of $\varepsilon < 10^{2.5}$ and $m < 1.5$ GeV that are competitive with the state of the art constraints made by [23] (ArgoNeuT). Further improvement of this study could show even better constraints, as the assumptions made throughout the analysis remained conservative.

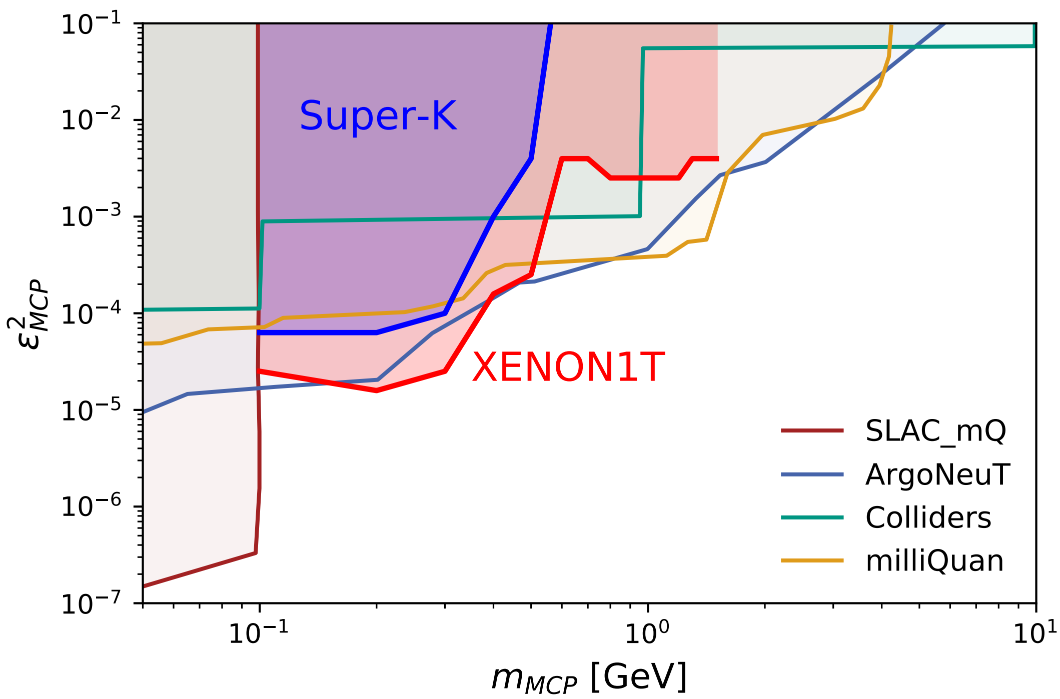

Figure 5.12: Constraints on MCPs as shown in Fig. 2.2. Shown in red are our constraints from the XENON1T analysis. Shown in blue are the constraints for Super-Kamiokande.

6. Summary and Outlook

The goal of this thesis was to find new competitive limits on millicharged particles (MCPs) in the mass range of $0.1\,\mathrm{GeV} \leq m \leq 100\,\mathrm{GeV}$ and charge range of $10^0 \leq \varepsilon \leq 10^{-4}$, where ε is the charge diminishing factor of the MCP charge $q_{MCP} = \varepsilon \cdot q_{el}$.

Traditionally, the search for MCPs was driven by beam-dump experiments, though in recent years searches for MCPs in cosmic rays and cosmic-ray air showers have become competitive and remain extremely promising. The enormous potential of cosmic-ray driven search for MCPs was illustrated and opportunities for further improvements have been explored.

Through a brief introcuction of the theoretical background of MCPs as a hypothetical conclusion of some physics beyond the standard model (BSM) theories, the main properties such as the mass- and charge range of interest and the major MCP production channels were clarified.

To study millicharged particles, the cosmic air shower simulation tool *MCEq* [8] was used to simulate the atmospheric flux of MCPs. As seen in other research, MCPs emerging from neutral meson decay of the pseudoscalar η meson as well as the vector mesons ρ^0, ω, ϕ and J/Ψ have been implemented in MCEq [9] [10]. Furthermore, through adding an improved electromagnetic shower model into MCEq, the MCP production from γ pair production was added as a second production channel for MCPs. This component was never studied before and holds major potential, as high energy photons can produce MCPs of high masses of up to $100\,\mathrm{GeV}$ and beyond, as opposed to a maximum MCP mass of $m \approx 1.5\,\mathrm{GeV}$ that can be achieved from J/Ψ vector meson decay. With the implementation of these two major MCP production channels, our analysis remains conservative. Additionally, the ionization and radiative energy losses of MCPs in air were studied and implemented into MCEq.

As a result of this first part of our analysis, the flux of MCPs at sea level in the mass- and charge range of interest could be simulated. The flux of MCPs has been found to decrease quickly for higher energies and higher masses. A comparison of different primary, atmospheric density and interaction models used by MCEq was made and the impact on the total MCP flux was discussed. The different models do not seem to have a large impact on the MCP flux, as their main differences appear in the high energy range, where the flux of MCPs is dwindling rapidly anyway.

In a thorough study of the particle propagation of MCPs through the Earth, a sophisticated Earth density model parametrization of the *Preliminary Reference Earth Model (PREM)* was introduced [11]. This model was used to calculate the energy losses of MCPs in matter on their way from their impact location on the Earth's surface to a detector location underground.

The resulting fluxes after decreasing due to ionization and radiative energy losses in matter were compared to calculations made in other research and were found to behave as expected.

To achieve constraints on MCPs in the charge-mass-plane, the expected signatures left by the simulated MCP fluxes were computed for the underground WIMP detector *XENON1T* [12] and the large neutrino experiment *Super-Kamiokande* [13]. The XENON1T detector was chosen as a promising source of new physics, as a small excess in recoil events has been found at low recoil energies that has yet to be explained. The detector signals were calculated assuming free electron scattering of MCPs.

By comparing the hypothetical signatures to the actual electron recoil signal of each detector through a statistical analysis, constraints on MCPs in the range of interest were found. To a small extent, these results show novel limits that are consistent with other research [9], and even exceed the currently existing limits on MCPs in a small mass space.

To conclude, the major improvements compared to previous MCP research made in this work were

- the implementation of photon pair production as a source of MCPs in MCEq using an improved model for the electromagnetic component of cosmic-ray air showers. This allows us to study even higher MCP masses in principle. However, current experimental data does not yet allow to exploit this fully.
- the actual simulation of MCPs through MCEq instead of using simple calculations. A much larger variety of models, assumptions and uncertainties can be tested through this attempt.
- the use of the complex Earth density model of the PREM. This concludes in a sophisticated study of MCP energy losses during their propagation through the Earth.
- the simultaneous cross-validation of the muon flux with existing data. Simulating the muon flux simultaneous to the MCP flux allows for a much better assessment of the obtained results.

The analysis in this thesis is very promising to be able to achieve even better results by applying further improvements in the future. Through comparison of the predicted muon flux made by MCEq with actual experimental data, a better understanding of the differences can improve the precision of the MCEq simulation to begin with. Other more exotic production channels for MCPs could be implemented to further improve the accuracy of the MCP flux, such as *Dalitz-Decays* [9]. The assumption of the free electron approximation made for the electron recoil signal could be replaced by a more sophisticated relativistic impulse approximation [61] to achieve more realistic results leading to higher fluxes and stronger limits. Also, it is possible to calculate more elaborate detector signatures such as multiple hit electron recoils, as seen in related research [9]. Furthermore, the statistical analysis used to determine new limits from the calculated MCP signals could be done for other detectors, eg. with larger fiducial target volumes to achieve a better sensitivity for the low fluxes of MCPs with higher masses. Detectors that could be used for a further analysis include *IceCube* [68] with its large target volume or *ArgoNeuT* [69], which has been used in other research regarding MCPs [10]. Future detectors could even be designed for a maximum reach for MCP searches.

The search for MCPs with cosmic ray data is a viable measurement, which can be nicely done be reusing data from low-background detectors. It will remain competitive and complementary to direct searches at colliders and beam-dump experiments.

The study of MCPs remains promising, as there are still wide mass and charge ranges unconstrained. HL-LHC in combination with cosmic-ray measurements will close the remaining gap in the search for MCPs with masses from 0.1 to 100GeV down to charges of

$\varepsilon < 10^{-4}$ within the next decade. The hypothetical existence of such particles fuels many BSM theories [6] [7] and their exclusion is a powerful tool to verify or falsify those theories.

Acknowledgements

First and foremost, I want to thank my supervisor Dr. Ralf Ulrich for his incredible support, especially in these last couple of weeks. He has always taken his time for my requests and has patiently answered all of my questions however dense they might have been. Working with someone as keen and present has been a blessing and frankly, tons of fun.

Secondly, I thank Prof. Dr. Ralph Engel, who agreed to be the first reviewer of this thesis and has given me great advice to accomplish and improve this study.

My further thanks goes to Dr. Anatoli Fedynitch, who has advised me frequently and has especially helped me handle MCEq.

Furthermore, I want to thank the whole CORSIKA group for their weekly support and their caring enthusiasm. In particular, I thank Antonio Augusto Alves Jr., Nikolaos Karastathis, Tanguy Pierog, Maximilian Reininghaus and Pranav Sampathkumar. Especially in times of the Corona pandemic, when we were only so rarely able to meet in person, they have made me feel involved and have always encouraged me.

In addition, I thank Dr. Klaus Eitel for his counsel on the XENON1T experiment.

Last but not least, I want to thank my friends and family, who have endured and endorsed me throughout my whole thesis (and also in the meantime). For their irreplacable support I want to especially thank Björn Graudejus for his unplanned lectorship, Michele Hebel for her motivational birdie, Maria Höver for her limitless spirit, Sebastian Kneipp for his IT support, Henrik Kuhn for his culinary offers, Marius Schmidt for his preserverance, Ellen Sarauer for her constant reassurance, and the whole Pokrandt bunch for basically everything.

Bibliography

[1] L. Baudis, "The search for dark matter," *European Review*, vol. 26, p. 70–81, Dec 2017.

[2] C. Arbeláez, R. Cepedello, R. M. Fonseca, and M. Hirsch, "(g 2) anomalies and neutrino mass," *Physical Review D*, vol. 102, Oct 2020.

[3] T. Aoyama, N. Asmussen, M. Benayoun, J. Bijnens, T. Blum, M. Bruno, I. Caprini, C. Carloni Calame, M. Cè, G. Colangelo, and et al., "The anomalous magnetic moment of the muon in the standard model," *Physics Reports*, vol. 887, p. 1–166, Dec 2020.

[4] T. K. Gaisser, "Outstanding problems in particle astrophysics," in *International School of Cosmic Ray Astrophysics: 14th Course: Neutrinos and Explosive Events in the Universe: A NATO Advanced Study Institute*, pp. 3–31, 1 2005.

[5] H. M. Lee, "Lectures on physics beyond the standard model," *Journal of the Korean Physical Society*, vol. 78, p. 985–1017, May 2021.

[6] L. B. Okun, "LIMITS OF ELECTRODYNAMICS: PARAPHOTONS?," *Sov. Phys. JETP*, vol. 56, p. 502, 1982.

[7] B. Holdom, "Two U(1)'s and Epsilon Charge Shifts," *Phys. Lett. B*, vol. 166, pp. 196–198, 1986.

[8] A. Fedynitch, "Cascade equations and hadronic interactions at very high energies," 2015.

[9] C. A. Argüelles, K. J. Kelly, and V. M. Muñoz, "Millicharged particles from the heavens: Single- and multiple-scattering signatures," 2021.

[10] R. Harnik, Z. Liu, and O. Palamara, "Millicharged particles in liquid argon neutrino experiments," *Journal of High Energy Physics*, vol. 2019, Jul 2019.

[11] A. M. Dziewonski and D. L. Anderson, "Preliminary reference earth model," *Physics of the Earth and Planetary Interiors*, vol. 25, no. 4, pp. 297–356, 1981.

[12] E. Aprile, J. Aalbers, F. Agostini, M. Alfonsi, F. D. Amaro, M. Anthony, B. Antunes, F. Arneodo, M. Balata, and et al., "The xenon1t dark matter experiment," *The European Physical Journal C*, vol. 77, Dec 2017.

[13] K. Bays, T. Iida, K. Abe, Y. Hayato, K. Iyogi, J. Kameda, Y. Koshio, L. Marti, M. Miura, S. Moriyama, and et al., "Supernova relic neutrino search at super-kamiokande," *Physical Review D*, vol. 85, Mar 2012.

[14] Wikipedia contributors, "Standard model — Wikipedia, the free encyclopedia." `https://en.wikipedia.org/w/index.php?title=Standard_Model&oldid=1037331085`, 2021. [Online; accessed 11-August-2021].

[15] C. Grupen, *Astroparticle Physics.* Springer, Cham, 2 ed., 2020.

[16] G. Shiu, P. Soler, and F. Ye, "Millicharged dark matter in quantum gravity and string theory," *Physical Review Letters*, vol. 110, Jun 2013.

[17] S. Abel and B. Schofield, "Brane–antibrane kinetic mixing, millicharged particles and susy breaking," *Nuclear Physics B*, vol. 685, p. 150–170, May 2004.

[18] E. Izaguirre and I. Yavin, "New window to millicharged particles at the lhc," *Physical Review D*, vol. 92, Aug 2015.

[19] F. Kahlhoefer and E. Urdshals, "On dark atoms, massive dark photons and millicharged sub-components," *Physics Letters B*, vol. 807, p. 135601, Aug 2020.

[20] R. Plestid, V. Takhistov, Y.-D. Tsai, T. Bringmann, A. Kusenko, and M. Pospelov, "Constraints on millicharged particles from cosmic-ray production," *Physical Review D*, vol. 102, Dec 2020.

[21] S. Davidson, S. Hannestad, and G. Raffelt, "Updated bounds on milli-charged particles," *Journal of High Energy Physics*, vol. 2000, p. 003–003, May 2000.

[22] A. A. Prinz, "The Search for millicharged particles at SLAC," other thesis, 3 2001.

[23] R. Acciarri, C. Adams, J. Asaadi, B. Baller, T. Bolton, C. Bromberg, F. Cavanna, D. Edmunds, R. Fitzpatrick, B. Fleming, and et al., "Improved limits on millicharged particles using the argoneut experiment at fermilab," *Physical Review Letters*, vol. 124, Apr 2020.

[24] R. Essig *et al.*, "Working Group Report: New Light Weakly Coupled Particles," in *Community Summer Study 2013: Snowmass on the Mississippi*, 10 2013.

[25] A. Ball, G. Beauregard, J. Brooke, C. Campagnari, M. Carrigan, M. Citron, J. De La Haye, A. De Roeck, Y. Elskens, R. E. Franco, and et al., "Search for millicharged particles in proton-proton collisions at s=13 tev," *Physical Review D*, vol. 102, Aug 2020.

[26] P. Zyla *et al.*, "Review of Particle Physics, Meson Summary Table," *PTEP*, vol. 2020, no. 8, pp. 41–92, 2020.

[27] M. Kachelrieß and J. Tjemsland, "Meson production in air showers and the search for light exotic particles," *Astroparticle Physics*, vol. 132, p. 102622, Nov 2021.

[28] L. Landsberg, "Electromagnetic decays of light mesons," *Physics Reports*, vol. 128, no. 6, pp. 301–376, 1985.

[29] G. Magill, R. Plestid, M. Pospelov, and Y.-D. Tsai, "Millicharged particles in neutrino experiments," *Phys. Rev. Lett.*, vol. 122, no. 7, p. 071801, 2019.

[30] Y.-S. Tsai, "Pair production and bremsstrahlung of charged leptons," *Rev. Mod. Phys.*, vol. 46, pp. 815–851, Oct 1974.

[31] H. Burkhardt, S. R. Kelner, and R. P. Kokoulin, "Monte Carlo generator for muon pair production," 5 2002.

[32] R. Nave, "Hyperphysics." `http://hyperphysics.phy-astr.gsu.edu/hbase/Astro/cosmic.html`. [Online; accessed 19-September-2021].

[33] J. Knapp, "Air shower simulations: Corsika." `https://www.zeuthen.desy.de/~jknapp/fs/proton-showers.html`. [Online; accessed 19-September-2021].

[34] P. Zyla *et al.*, "Review of Particle Physics, 30. Cosmic Rays," *PTEP*, vol. 2020, no. 8, pp. 510–518, 2020.

[35] A. Aab, P. Abreu, M. Aglietta, *et al.*, "Measurement of the cosmic-ray energy spectrum above 2.5×10^{18} eV using the pierre auger observatory," *Phys. Rev. D*, vol. 102, p. 062005, Sep 2020.

[36] P. Lipari, "Lepton spectra in the earth's atmosphere," *Astroparticle Physics*, vol. 1, no. 2, pp. 195–227, 1993.

[37] A. Fedynitch, R. Engel, T. K. Gaisser, F. Riehn, and T. Stanev, "Calculation of conventional and prompt lepton fluxes at very high energy," 2015.

[38] A. Fedynitch, "github.com//afedynitch/mceq." `https://github.com/afedynitch/MCEq.git`.

[39] A. Fedynitch, "readthedocs/readthedocs." `https://mceq.readthedocs.io/en/latest/tutorial.html`.

[40] F. Riehn, H. P. Dembinski, R. Engel, A. Fedynitch, T. K. Gaisser, and T. Stanev, "The hadronic interaction model sibyll 2.3c and feynman scaling," 2017.

[41] F. Riehn, R. Engel, A. Fedynitch, T. K. Gaisser, and T. Stanev, "Hadronic interaction model sibyll 2.3d and extensive air showers," *Physical Review D*, vol. 102, Sep 2020.

[42] S. Roesler, R. Engel, and J. Ranft, "The monte carlo event generator dpmjet-iii," *Advanced Monte Carlo for Radiation Physics, Particle Transport Simulation and Applications*, p. 1033–1038, 2001.

[43] T. K. Gaisser and A. M. Hillas, "Reliability of the method of constant intensity cuts for reconstructing the average development of vertical showers," *Intenational Cosmic Ray Conference, 15th, Plodiv, Bulgaria*, 1977.

[44] N. Aeronautics, N. O. Space Admisitration (NASA), A. A. (NOAA), and U. A. Force, "U.s. standard atmosphere 1976," *NASA technical report NASA-TM-X-74335, NOAA technical report NOAA-S/T-76-1562*, 1976.

[45] S. Meighen-Berger, A. Fedynitch, and M. Huber, "Emca – electromagnetic-cascades simulation package," 2019.

[46] P. Zyla *et al.*, "Review of Particle Physics, 43. Monte Carlo particle numbering scheme (rev.)," *PTEP*, vol. 2020, no. 8, pp. 560–563, 2020.

[47] J.-H. Koehne, K. Frantzen, M. Schmitz, T. Fuchs, W. Rhode, D. Chirkin, and J. Becker Tjus, "Proposal: A tool for propagation of charged leptons," *Computer Physics Communications*, vol. 184, no. 9, pp. 2070–2090, 2013.

[48] T. K. Gaisser, R. Engel, and E. Resconi, *Cosmic Rays and Particle Physics*. Cambridge University Press, 2 ed., 2016.

[49] P.-K. Hu, A. Kusenko, and V. Takhistov, "Dark cosmic rays," *Physics Letters B*, vol. 768, p. 18–22, May 2017.

[50] J. Reichenbacher, "Calculation of the underground muon intensity crouch curve from a parameterization of the flux at surface," 2007.

[51] T. K. Gaisser, "Spectrum of cosmic-ray nucleons, kaon production, and the atmospheric muon charge ratio," *Astroparticle Physics*, vol. 35, p. 801–806, Jul 2012.

[52] H. P. Dembinski, R. Engel, A. Fedynitch, T. Gaisser, F. Riehn, and T. Stanev, "Data-driven model of the cosmic-ray flux and mass composition from 10 GeV to 10^{11} GeV," *PoS*, vol. ICRC2017, p. 533, 2018.

[53] A. Fedynitch, J. Becker Tjus, and P. Desiati, "Influence of hadronic interaction models and the cosmic ray spectrum on the high energy atmospheric muon and neutrino flux," *Phys. Rev. D*, vol. 86, p. 114024, Dec 2012.

[54] R. Gandhi, C. Quigg, M. Hall Reno, and I. Sarcevic, "Ultrahigh-energy neutrino interactions," *Astroparticle Physics*, vol. 5, p. 81–110, Aug 1996.

[55] E. V. Bugaev, A. Misaki, V. A. Naumov, T. S. Sinegovskaya, S. I. Sinegovsky, and N. Takahashi, "Atmospheric muon flux at sea level, underground, and underwater," *Physical Review D*, vol. 58, Jul 1998.

[56] V. C. Wilson, "Cosmic-ray intensities at great depths," *Phys. Rev.*, vol. 53, pp. 337–343, Mar 1938.

[57] P. H. Barrett, L. M. Bollinger, G. Cocconi, Y. Eisenberg, and K. Greisen, "Interpretation of cosmic-ray measurements far underground," *Rev. Mod. Phys.*, vol. 24, pp. 133–178, Jul 1952.

[58] C. Castagnoli, A. De Marco, A. Longhetto, and P. Penego, "Il nuovo cimento," 1965.

[59] J. N. Crookes and B. C. Rastin, "The absolute intensity of muons at 31.6 hg (1/cm-squared) below sea-level," *Nucl. Phys. B*, vol. 58, pp. 93–109, 1973.

[60] M. Aglietta, E. Alyea, P. Antonioli, *et al.*, "Study of single muons with the large volume detector at the gran sasso laboratory," *Phys. Atom. Nuclei*, vol. 66, Jan 2003.

[61] C.-K. Qiao, S.-T. Lin, H.-C. Chi, and H.-T. Jia, "Relativistic impulse approximation in the atomic ionization process induced by millicharged particles," *Journal of High Energy Physics*, vol. 2021, Mar 2021.

[62] NWO-I, "Xenon1t." `https://www.nwo-i.nl/en/xenon1t-2/`. [Online; accessed 27-September-2021].

[63] X. Collaboration, E. Aprile, J. Aalbers, F. Agostini, M. Alfonsi, F. Amaro, M. Anthony, F. Arneodo, P. Barrow, L. Baudis, B. Bauermeister, M. L. Benabderrahmane, T. Berger, P. Breur, A. Brown, E. Brown, S. Bruenner, G. Bruno, R. Budnik, and S. Nisi, "Material radioassay and selection for the xenon1t dark matter experiment," *The European Physical Journal C*, vol. 77, 05 2017.

[64] E. Aprile, J. Aalbers, F. Agostini, M. Alfonsi, L. Althueser, F. Amaro, V. Antochi, E. Angelino, J. Angevaare, F. Arneodo, and et al., "Excess electronic recoil events in xenon1t," *Physical Review D*, vol. 102, Oct 2020.

[65] K. Collaboration, K. Abe, C. Bronner, Y. Hayato, *et al.*, "Diffuse supernova neutrino background search at super-kamiokande," 2021.

[66] M. Renner, "Der super kamiokande detektor." `http://www-ekp.physik.uni-karlsruhe.de/~jwagner/SS08/talks/MichaelRenner.pdf`. [Online; accessed 27-September-2021].

[67] V. Blobel, "Data fitting." `https://www.desy.de/~sschmitt/blobel/blobel_fitting.pdf`, 2005. [Online; accessed 27-September-2021].

[68] D. R. Williams, "Results from icecube," 2019.

[69] C. Anderson, M. Antonello, B. Baller, T. Bolton, C. Bromberg, F. Cavanna, E. Church, D. Edmunds, A. Ereditato, S. Farooq, and et al., "The argoneut detector in the numi low-energy beam line at fermilab," *Journal of Instrumentation*, vol. 7, p. P10019–P10019, Oct 2012.